Article

Allosteric modulation and biased signalling at free fatty acid receptor 2

https://doi.org/10.1038/s41586-025-09186-6

Received: 8 August 2024

Accepted: 22 May 2025

Published online: 18 June 2025

Check for updates

Xuan Zhang[1,5], Abdul-Akim Guseinov[2,3,5], Laura Jenkins[3,5], Alice Valentini[4], Sara Marsango[3], Katrine Schultz-Knudsen[4], Trond Ulven[4], Elisabeth Rexen Ulven[4], Irina G. Tikhonova[2]✉, Graeme Milligan[3]✉ & Cheng Zhang[1]✉

Free fatty acid receptor 2 (FFA2) is a G protein-coupled receptor (GPCR) that is a primary sensor for short-chain fatty acids produced by gut microbiota. Consequently, FFA2 is a promising drug target for immunometabolic disorders[1–4]. Here we report cryogenic electronic microscopy structures of FFA2 in complex with two G proteins and three distinct classes of positive allosteric modulators (PAMs), and describe noncanonical activation mechanisms that involve conserved structural features of class A GPCRs. Two PAMs disrupt the E/DRY activation microswitch[5] and stabilize the conformation of intracellular loop 2 by binding to lipid-facing pockets near the cytoplasmic side of the receptor. By contrast, the third PAM promotes the separation of transmembrane helices 6 and 7 by interacting with transmembrane helix 6 at the receptor–lipid interface. Molecular dynamic simulations and mutagenesis experiments confirm these noncanonical activation mechanisms. Furthermore, we demonstrate the molecular basis for the G_i versus G_q bias, which is due to distinct conformations of intracellular loop 2 stabilized by different PAMs. These findings provide a framework for the design of tailored GPCR modulators, with implications that extend beyond FFA2 to the broader field of GPCR drug discovery.

In humans, short-chain fatty acids (SCFAs), including acetate (C2), propionate (C3) and butyrate (C4), are produced during the anaerobic fermentation of dietary fibre by gut microbiota and substantially affect health[4]. SFCAs can activate several GPCRs. Among these, FFA2 (also known as GPR43) and FFA3 (also known as GPR41) are the primary SCFA receptors[1,3,6]. Extensive research has shown that many beneficial effects of gut microbiota, such as resolving inflammation[7], limiting fat accumulation[8] and defending against pathogens[9,10], are mediated through SCFA–FFA2 signalling pathways by interacting with β-arrestins and the $G_{i/o}$ and $G_{q/11}$ families of G proteins[1,6] (Fig. 1a). Consequently, FFA2 has emerged as a promising therapeutic target for metabolic disorders such as obesity and diabetes[2,11,12] and for inflammatory diseases[4,13,14].

Despite the therapeutic significance of FFA2, the development of effective orthosteric agonists has proven challenging, as evidenced by the scarcity of reported synthetic FFA2 agonists. The compound (2*R*,4*R*)-2-(2-chlorophenyl)-3-(4-(3,5-dimethylisoxazol-4-yl)benzoyl) thiazolidine-4-carboxylic acid (TUG-1375) (Fig. 1b) is one of the few reported[15]. Three distinct series of allosteric activators (or PAMs) of FFA2 have also emerged from research in the pharmaceutical industry. A group of phenylacetamides developed by Amgen[16], particularly 4-chloro-α-(1-methylethyl)-*N*-2-thiazolylbenzeneacetamide (4-CMTB)[17] (Fig. 1b), has become widely used in studies of FFA2 (refs. 6,18). AstraZeneca reported *N*-[3-(2-carbamimidamido-4-methyl-1,3-thiazol-5-yl) phenyl]-4-fluorobenzamide (AZ-1729) (Fig. 1b) as a G_i-biased allosteric activator[19]. More recently, 4-[(2*R*,6*S*)-2,6-dimethylmorpholin-4-yl]-7-(2-fluorobenzenesulfonyl)-2-methyl-5*H*-pyrrolo[3,2-*d*]pyrimidin-6-amine (compound 187)[20] (Fig. 1b), from a patent filed by Takeda, showed modest effects in a mouse model of colitis induced by dextran sodium sulfate[14]. These three FFA2 PAMs do not share a clear conserved chemical scaffold.

We previously reported a high-resolution cryogenic electron microscopy (cryo-EM) structure of C4 bound to the human FFA2 signalling complex[21]. Another group recently reported a structure of FFA2 bound to TUG-1375 (ref. 22), which occupies the same binding pocket as C4. However, the binding locations and functional mechanisms of various PAMs remain unknown, with previous homology modelling and mutagenesis efforts proving inconclusive. Here we report cryo-EM structures of multiple human FFA2 signalling complexes with three PAMs and the orthosteric agonist TUG-1375. Our structures, together with pharmacological studies, functional analyses and molecular dynamic (MD) simulations, reveal distinct allosteric sites for the three PAMs. We also describe mechanisms of noncanonical activation and G-protein-subtype-selective signalling of FFA2.

Signalling and pharmacology of agonists and PAMs

Orthosteric agonists of FFA2, including TUG-1375 and the endogenous SCFA C3 (Fig. 1b), promote interactions with G_i and G_q heterotrimeric G proteins[23] and β-arrestins[24]. Among the three chemically distinct

[1]Department of Pharmacology and Chemical Biology, School of Medicine, University of Pittsburgh, Pittsburgh, PA, USA. [2]School of Pharmacy, Queen's University Belfast, Belfast, UK. [3]Centre for Translational Pharmacology, School of Molecular Biosciences, College of Medical, Veterinary and Life Sciences, University of Glasgow, Glasgow, UK. [4]Department of Drug Design and Pharmacology, Faculty of Health and Medical Sciences, University of Copenhagen, Copenhagen, Denmark. [5]These authors contributed equally: Xuan Zhang, Abdul-Akim Guseinov, Laura Jenkins. ✉e-mail: i.tikhonova@qub.ac.uk; graeme.milligan@glasgow.ac.uk; chengzh@pitt.edu

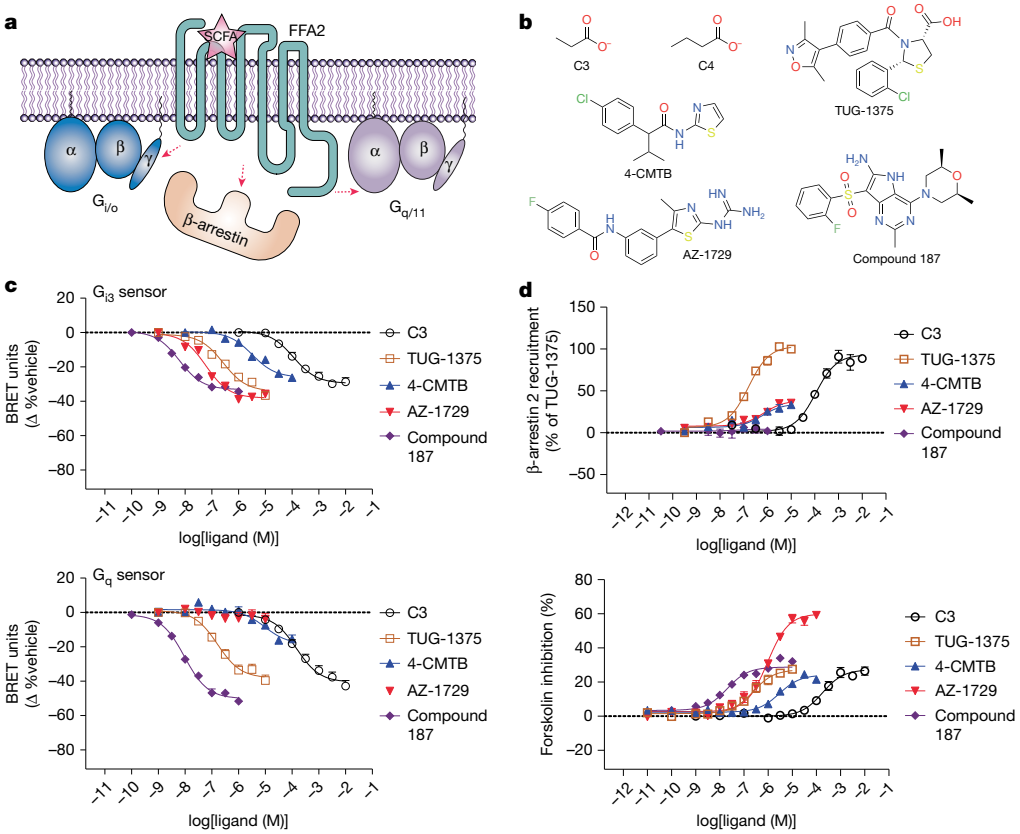

Fig. 1 | Structure and function of FFA2 activators and modulators. **a**, Schematic of how FFA2 senses SCFAs to activate multiple signalling partners, including β-arrestins and the $G_{i/o}$ and $G_{q/11}$ families of G proteins. **b**, Chemical structures of FFA2 activators and modulators. **c**, Quantification of the activation of G_{i3} and G_q TRUPATH sensors induced by FFA2 activators and modulators. BRET, bioluminescence resonance energy transfer. **d**, Quantification of β-arrestin 2 recruitment and inhibition of forskolin-stimulated levels of cAMP induced by FFA2 activators and modulators. For **c** and **d**, data are the mean ± s.e.m. $n = 3$ (3 biologically independent experiments).

allosteric modulators of FFA2—4-CMTB[16,17,25], AZ-1729 (refs. 19,26) and compound 187 (ref. 14) (Fig. 1b)—4-CMTB signals through both G_i and G_q pathways[16], whereas AZ-1729 displays unusual G protein selectivity, with a bias towards G_i over G_q (ref. 19). The signalling profile of compound 187 has been only partially characterized[14].

Using TRUPATH G protein sensors[27] in HEK293T cells, we characterized the signalling profiles of FFA2 ligands. C3 activated both G_{i3} and G_q with modest potency, whereas TUG-1375 showed similar activation of both G protein sensors, but with around 1,000 times higher potency than C3 (Fig. 1c). Compound 187 was the most potent ligand tested and it effectively activated both G protein subtypes (Fig. 1c). 4-CMTB activated both G_{i3} and G_q, but with modest efficacy (Fig. 1c). By contrast, AZ-1729 potently activated G_{i3} with high efficacy but showed minimal G_q activation (Fig. 1c). Our results confirm that all three FFA2 PAMs function as allosteric agonists (ago-PAMs).

We then assessed the ability of these ligands to recruit β-arrestins. C3 and TUG-1375 effectively recruited both β-arrestin 1 (Extended Data Fig. 1a) and β-arrestin 2 (Fig. 1d), and TUG-1375 was around 1,000 times more potent than C3. AZ-1729 and 4-CMTB acted as partial agonists, with modest efficacy for both β-arrestin types, whereas compound 187 did not display detectable activity in these assays (Fig. 1d and Extended Data Fig. 1a). All ligands reduced forskolin-amplified cAMP levels in Flp-In T-REx 293 cells stably expressing human FFA2 linked to eYFP. The following potency ranking was observed: compound 187 > TUG-1375 > AZ-1729 ≥ 4-CMTB > C3 (Fig. 1d). Notably, AZ-1729 showed greater efficacy than the other allosteric and orthosteric activators in this assay (Fig. 1d). These results demonstrate that compound 187 favours G protein activation over β-arrestin recruitment, whereas AZ-1729 preferentially activates G_i over G_q while retaining partial efficacy for β-arrestin recruitment. 4-CMTB also exhibited modest selectivity for G_i over G_q (Fig. 1c). Of note, β-arrestin 2 recruitment occurred at similar levels in wild-type HEK293T cells and G-protein-deficient HEK293T cells. This finding indicates a G-protein-independent mechanism for FFA2 to recruit β-arrestins (Extended Data Fig. 1b).

For subsequent studies, we used multiple assay types to validate roles of key FFA2 residues in ligand interactions and receptor function across various human FFA2 complexes. These assays included the measurement of G_i-mediated cAMP reduction and β-arrestin recruitment, [^{35}S]GTPγS-binding assays and FFA2 radioligand-binding assays using the antagonist [^{3}H]GLPG0974 (ref. 28).

Next, we examined cooperative effects between the allosteric modulators and TUG-1375 using cAMP-reduction assays (Extended Data Fig. 1d). 4-CMTB enhanced the potency of TUG-1375 without affecting maximal efficacy (Fig. 2a), whereas compound 187 markedly increased the efficacy of TUG-1375 without altering potency (Fig. 2a). AZ-1729 increased both the potency and efficacy of TUG-1375 (Fig. 2a), and TUG-1375 reciprocally enhanced the potency and efficacy of AZ-1729 (Fig. 2a). 4-CMTB also enhanced the potency of AZ-1729 (Fig. 2b) and the efficacy of compound 187 (Fig. 2b), a result that suggested that these compounds bind at nonoverlapping sites. However, compound 187 did not show functional cooperativity with AZ-1729 (Fig. 2b), which suggests that they may share overlapping binding sites. Binding affinity (pK_i) estimates ranged from 6.25 to 6.41 for TUG-1375, from 5.53 to 6.22 for 4-CMTB and from 5.89 to 6.08 for AZ-1729 (Extended Data Fig. 1d). All PAMs exhibited similar allosteric modulation with the endogenous ligand C3 as with TUG-1375 (Extended Data Fig. 1c,d).

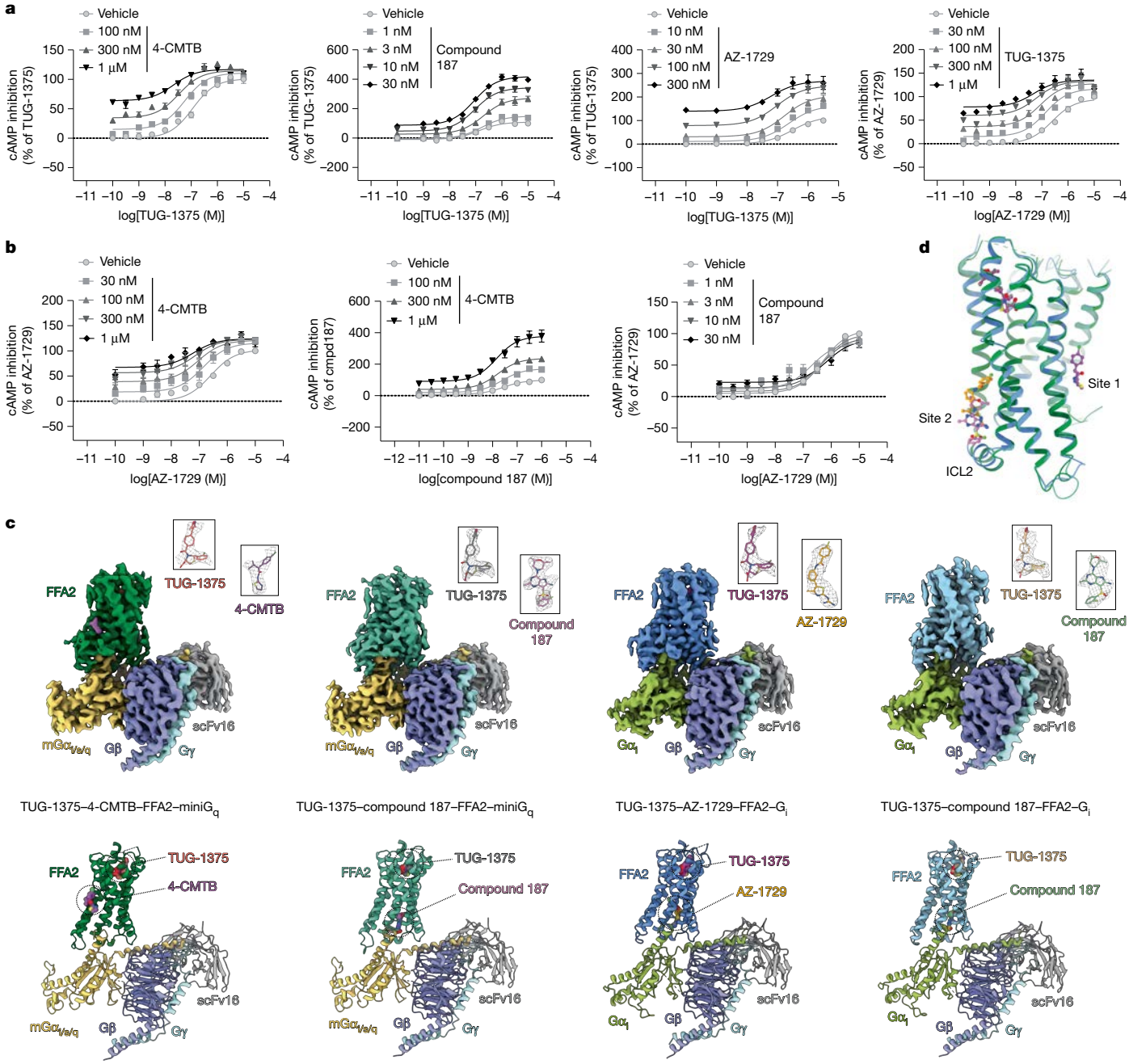

Fig. 2 | Cooperativity of function between various FFA2 modulators and overall structures of FFA2 with diverse modulators. a, Cooperativity of function between three FFA2 PAMs and the orthosteric agonist TUG-1375. The ability of the indicated concentrations of 4-CMTB, compound 187 and AZ-1729 to modulate the inhibition of forskolin-stimulated levels of cAMP through FFA2 is shown. The cooperative effects of AZ-1729 and TUG-1375 displayed reciprocity. **b**, Cooperativity of function between the three FFA2 ago-PAMs. The ability of the indicated concentrations of 4-CMTB to modulate the function of AZ-1729 and compound 187 is displayed. Different concentrations of compound 187 do not modulate the effects of AZ-1729. For **a** and **b**, data are the mean ± s.e.m. $n = 3$ (3 biologically independent experiments). **c**, Cryo-EM maps (top row) and structural models (bottom row) of TUG-1375-bound FFA2 signalling complexes, including 4-CMTB–FFA2 (forest green) and compound 187–FFA2 (green) in complex with miniG$_q$, and AZ-1729–FFA2 (blue) and compound 187–FFA2 (turquoise) in complex with G$_i$. mGα$_{i/s/q}$, Gα$_i$, Gβ and Gγ subunits are coloured in dark yellow, green-yellow, purple and pale turquoise, respectively. ScFv16 is in dark grey. The clear cryo-EM density maps of all ligands are shown as meshes in the insets of the top row. **d**, Superimposition of FFA2 bound to three ago-PAMs showing site 1 and the upper and lower regions of site 2 for 4-CMTB, AZ-1729 and compound 187, respectively.

Structures of human FFA2 signalling complexes

The diverse signalling profiles and cooperativity patterns of FFA2 PAMs suggest that they have distinct modes of receptor modulation, which may be associated with different binding sites. To investigate the allosteric modulation mechanism of FFA2, we determined cryo-EM structures of G$_q$-coupled FFA2 in complex with TUG-1375 and 4-CMTB or compound 187 and of G$_i$-coupled FFA2 in complex with TUG-1375 and AZ-1729 or compound 187 at global nominal resolutions of 3.1–3.4 Å (Fig. 2c, Extended Data Table 1 and Extended Data Fig. 2). For the G$_q$-coupled complexes, we used miniG$_q$ (refs. 21,29–31), which contains an engineered α-subunit (Gα$_q$) referred to as mGα$_{i/s/q}$ (refs. 32,33), to stabilize the complexes. To further stabilize the FFA2 and G protein complexes, we used the NanoBit tethering strategy[34].

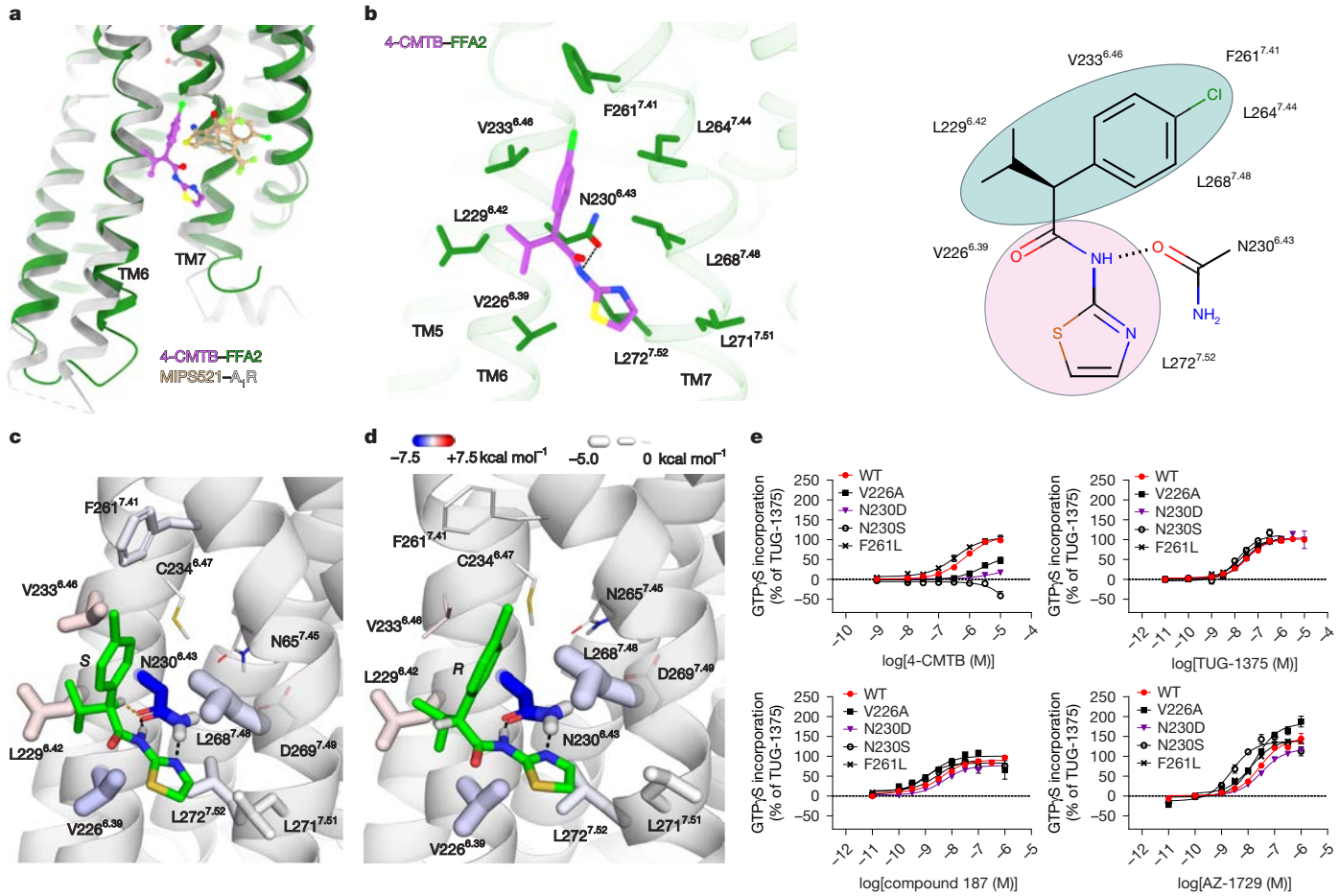

Fig. 3 | Binding of 4-CMTB in site 1. a, Superimposition of 4-CMTB–FFA2 with A_1R bound to the PAM MIPS521 (Protein Data Bank (PDB) accession 7LD3). Compared with MIPS521, 4-CMTB binds more superficially. **b**, Details of the interactions between 4-CMTB and FFA2 at site 1. **c**,**d**, Simulation snapshot depicting the (*S*) isomer of 4-CMTB (**c**) and the less active (*R*) isomer of 4-CMTB (**d**) in site 1, with protein residues shown as sticks. 4-CMTB is shown as green sticks. Carbon colours and stick thickness represent the simulation-averaged energies of electrostatic and van der Waals interactions of each residue with the ligand, respectively. Classical and nonclassical hydrogen bonds with $N230^{6.43}$ are indicated by dashed lines. The results illustrate the inability of (*R*) 4-CMTB to form a nonclassical hydrogen bond with $N230^{6.43}$ and the poor steric fit of its isopropyl (i-Pr) fragment. **e**, Effects of various mutations in site 1 of FFA2 on the function of FFA2 ligands measured in [^{35}S]GTPγS-binding assays. 4-CMTB is unable to promote the binding of [^{35}S]GTPγS at N230D and N230S FFA2, but other ligands are unaffected. Data are the mean ± s.e.m. $n = 3$ (3 biologically independent experiments). WT, wild type.

This approach involves the fusion of the two components of NanoBit to the carboxy-terminal ends of FFA2 and G_β and the single-chain variable fragment antibody scFv16, which was developed to stabilize the G_i heterotrimer[35].

The well-resolved cryo-EM maps enabled us to model most of the side chains of the receptor, the G proteins, scFv16 and TUG-1375 (Fig. 2c). Moreover, three distinct density maps were identified and assigned to the three PAMs (Fig. 2c). The structures revealed that 4-CMTB binds to an interhelical allosteric site near transmembrane helix 6 (TM6), whereas AZ-1729 and compound 187 occupy overlapping but nonidentical interhelical allosteric sites above intracellular loop 2 (ICL2) (Fig. 2d). The receptor and compound 187 exhibited high structural similarity, with no significant differences when coupled to miniG_q or G_i. To analyse the binding mechanism of compound 187 in more detail, we primarily focused on the miniG_q-coupled FFA2 complex with TUG-1375 and compound 187 owing to the better cryo-EM density map obtained for this structure than with the other complexes.

The transmembrane domain and extracellular loops of FFA2 closely matched the recently published TUG-1375-bound FFA2 structure[22] but differed from those in our previously published C4-bound structure[21] (Extended Data Fig. 3a). Mutagenesis studies confirmed the identity of the essential binding-pocket residues for TUG-1375 (Extended Data Fig. 3b). We also performed microsecond-scale classical MD simulations, which indicated the presence of a flexible orthosteric binding pocket to accommodate the large synthetic agonist (Extended Data Fig. 3c).

Binding of ago-PAMs at distinct allosteric sites

Our pharmacological studies showed that 4-CMTB enhances the action and/or potency of both AZ-1729 and compound 187 at FFA2 (Fig. 2b), which suggests that these ago-PAMs have nonoverlapping allosteric sites. Indeed, our cryo-EM structures revealed that 4-CMTB binds to site 1, an allosteric site at the membrane interface of TM6, whereas AZ-1729 and compound 187 bind to the upper and lower regions, respectively, of site 2 immediately above ICL2 (Fig. 2d).

Binding of 4-CMTB at site 1

The identified 4-CMTB-binding site, referred to as site 1, was unexpected based on previous modelling and mutagenesis efforts[17,36,37]. This site is adjacent to a known allosteric site in the adenosine A_1 receptor (A_1R) for the PAM MIPS521 (ref. 38). MIPS521 occupies a concave pocket between TM6 and TM7 of A_1R, whereas 4-CMTB binds more superficially near TM6 of FFA2 (Fig. 3a). In this membrane-embedded

site 1, 4-CMTB forms a single hydrogen bond with N230$^{6.43}$ (superscripts represent Ballesteros–Weinstein numbering[39]) (Fig. 3b). Such limited polar interactions are characteristic of allosteric GPCR ligands at membrane–receptor interfaces[40], where the membrane environment strengthens polar contacts[41]. MD simulations revealed that 4-CMTB engages the N230$^{6.43}$ side chain through both its amide and thiazole nitrogen atoms, acting as a hydrogen-bond donor and acceptor, respectively (Fig. 3c). An additional nonclassical C–H and O hydrogen bond is formed between the N230$^{6.43}$ side-chain oxygen (acceptor) and the C–H group at the chiral centre of 4-CMTB (donor) (Fig. 3c). Although weaker than conventional hydrogen bonds, such C–H···O interactions are increasingly gaining recognition as important contributors to protein–ligand binding, particularly when the C–H donor is adjacent to electron-withdrawing groups that increase its polarity. Such interactions are enhanced by the low dielectric constant of the membrane environment[41]. MD simulations showed that the substantially less active (*R*) isomer of 4-CMTB cannot form this interaction owing to geometric constraints, which contribute to its poor fit in the binding cavity (Fig. 3d). Further stabilization of 4-CMTB arises from van der Waals contacts with the surrounding residues V226$^{6.39}$, L229$^{6.42}$, V233$^{6.46}$, L264$^{7.44}$, L268$^{7.48}$ and L272$^{7.52}$ (Fig. 3b,c).

The dual 4-CMTB N230$^{6.43}$ hydrogen bonds validate previous structure–activity relationship (SAR) findings[17,25]. The following key structural requirements were identified: an essential amide hydrogen bond donor (N-methylation reduces potency by 120-fold); a crucial position-2 hydrogen-bond acceptor in the heterocycle (2-pyridyl preserves activity, whereas 3/4-pyridyl reduces it); and introduction of a carbonyl group decreases activity owing to reduced acceptor properties[17,25]. The following additional SAR data supported the binding mode of 4-CMTB: the low potency of pH-sensitive molecules aligns with the membrane location; the bulk tolerance of the 2,5-thiazole fragment matches its orientation towards TM7; the strict requirements for amide-adjacent alkyl groups reflect its proximity to TM6; the preference for a hydrogen between the amide and aromatic fragment indicates nonclassical hydrogen bonding; and the low polarity preference for the 4-chlorophenyl moiety confirms its deep membrane positioning[17,25].

The observed ligand–receptor interactions were also supported by mutagenesis studies. Alteration of N230$^{6.43}$ to aspartic acid, which allows only one hydrogen bond with 4-CMTB, eliminated both direct activation of human FFA2 by 4-CMTB (Fig. 3e and Extended Data Table 2a) and its cooperative effect on the potency of TUG-1375 (Extended Data Fig. 4a). Similarly, replacing N230$^{6.43}$ with serine, which disrupts hydrogen bonding with 4-CMTB, also abolished the agonistic action of 4-CMTB (Fig. 3e and Extended Data Table 2a). However, both mutations preserved the potency and efficacy of TUG-1375, compound 187 and AZ-1729, a result that confirmed that the mutant receptors maintained their overall structure and function (Fig. 3e and Extended Data Table 2a). Moreover, compound 187 and AZ-1729 retained their PAM effects on TUG-1375 at the N230$^{6.43}$D mutation of FFA2 (Extended Data Fig. 4a), and binding affinity for the antagonist [^{3}H]GLPG0974 was maintained (Extended Data Fig. 4a). Beyond N230$^{6.43}$, the mutation of V226$^{6.39}$ in FFA2 to alanine significantly reduced the agonistic activity of 4-CMTB on FFA2, whereas TUG-1375 and the other two ago-PAMs were minimally affected (Fig. 3e and Extended Data Table 2a). By contrast, replacing F261$^{7.41}$, which does not form direct interactions with 4-CMTB in our structure, with leucine had little effect on the activity of 4-CMTB (Fig. 3e and Extended Data Table 2a). In FFA3, although N$^{6.43}$ is conserved, notable variations in the 4-CMTB-binding pocket resulted in a distinct configuration of site 1 in FFA3. These changes included the replacement of V226$^{6.39}$ in FFA2 by A229$^{6.39}$ in FFA3 and significant conformational variations of the conserved residues L$^{6.42}$ and L$^{7.44}$ between FFA2 and FFA3 (Extended Data Fig. 4b). These differences probably explain the high selectivity of 4-CMTB for FFA2 compared with FFA3.

Binding of AZ-1729 and compound 187 at site 2

As the pharmacology studies and docking findings indicated that AZ-1729 and compound 187 do not share binding sites with 4-CMTB, we predicted their locations using cosolvent simulation techniques for membrane proteins[42]. The simulations revealed strong interactions between the probes and E106$^{3.49}$ (Extended Data Fig. 4c). We then docked both ligands to the induced-fit receptor conformation from these simulations. In agreement with our predictions, the cryo-EM structures showed that AZ-1729 and compound 187 bind to site 2, another allosteric site located above ICL2, and occupy the upper and the lower regions in this site, respectively (Fig. 4a,b). Both regions are formed by residues from TM2–TM5 and ICL2. AZ-1729 sits further from ICL2 than compound 187, with a slightly smaller allosteric binding pocket (1,318 Å^2 for AZ-1729 compared with 1,607 Å^2 for compound 187) (Fig. 4c). In both miniG_q-coupled and G_i-coupled FFA2 structures with compound 187, the site 2 conformation, including ICL2, were nearly identical (Extended Data Fig. 4d).

AZ-1729 occupies the upper region of site 2, with its guanidyl moiety oriented towards ICL2 and the rest of the molecule extending towards the centre of the seven transmembrane bundle and reaching W98$^{3.41}$ (Fig. 4a). The guanidyl moiety of AZ-1729, critical for ligand binding, forms two hydrogen bonds with E106$^{3.49}$ (Fig. 4a). Similarly, in the lower region of site 2, compound 187 forms polar interactions with E106$^{3.49}$ (Fig. 4b).

In support of these structural observations, both AZ-1729 and compound 187 did not show detectable activity at the E106$^{3.49}$G residue of FFA2 in cAMP-inhibition assays (Fig. 4d and Extended Data Table 2b). Moreover, they displayed reduced efficacy in [^{35}S]GTPγS-binding assays (Extended Data Table 2c and Extended Data Fig. 4e), whereas TUG-1375 and 4-CMTB functioned normally at this mutant receptor (Extended Data Table 2b,c and Extended Data Fig. 4e). MD simulations confirmed that both ligands extensively interact with E106$^{3.49}$ (Fig. 4e) and prevent its interaction with R107$^{3.50}$ of the conserved ionic lock (E/D)R$^{3.50}$Y motif$^{5.43}$ in the absence of G proteins (Fig. 4f).

Furthermore, AZ-1729 either lacked detectable function or displayed around 100-fold reduced potency at the G102$^{3.45}$V residue of FFA2 (Fig. 4d, Extended Data Table 2b,c and Extended Data Fig. 4e), located one turn of TM3 above E106$^{3.49}$. This alteration is anticipated to cause steric hindrance for the binding of AZ-1729. Compound 187 retained activity at G102$^{3.45}$V, but with 10–30-fold reduced potency, whereas both TUG-1375 and 4-CMTB showed unaltered potency (Fig. 4d, Extended Data Table 2b,c and Extended Data Fig. 4e). Although AZ-1729 displayed only modest efficacy compared with TUG-1375 in β-arrestin 2 recruitment assays with wild-type FFA2–eYFP (Fig. 1d), this result was sufficient for additional assessments, which confirmed the loss of response to AZ-1729 at both E106$^{3.49}$G and G102$^{3.45}$V residues in FFA2 (Extended Data Fig. 4f).

We further explored alterations around the binding pocket of site 2. The A129$^{4.45}$V mutation substantially reduced the potency of both compound 187 and AZ-1729 in [^{35}S]GTPγS-binding assays, whereas no effect was seen for TUG-1375 or 4-CMTB (Extended Data Table 2c and Extended Data Fig. 4e). However, significance was only reached for compound 187 in the cAMP assays (Fig. 4d and Extended Data Table 2a). Even though MD simulations indicated cation–π interactions between the guanidyl group of AZ-1729 and Y125$^{4.41}$ and π interactions between this residue and the 5,7-diazaindole of compound 187 (Fig. 4e), the Y125$^{4.41}$Q mutation did not significantly affect potencies (Extended Data Table 2c). However, large reductions in potency for both compound 187 and AZ-1729 were observed when the adjacent residue G126$^{4.42}$ was changed to serine (Extended Data Table 2b,c). Notably, the L47$^{2.42}$Y mutation eliminated responses to compound 187 and substantially reduced the potency for AZ-1729 (Extended Data Table 2b,c). Consistent with the positioning of the 2-fluorophenyl moiety of compound 187, the F113$^{3.56}$A mutation resulted in a larger

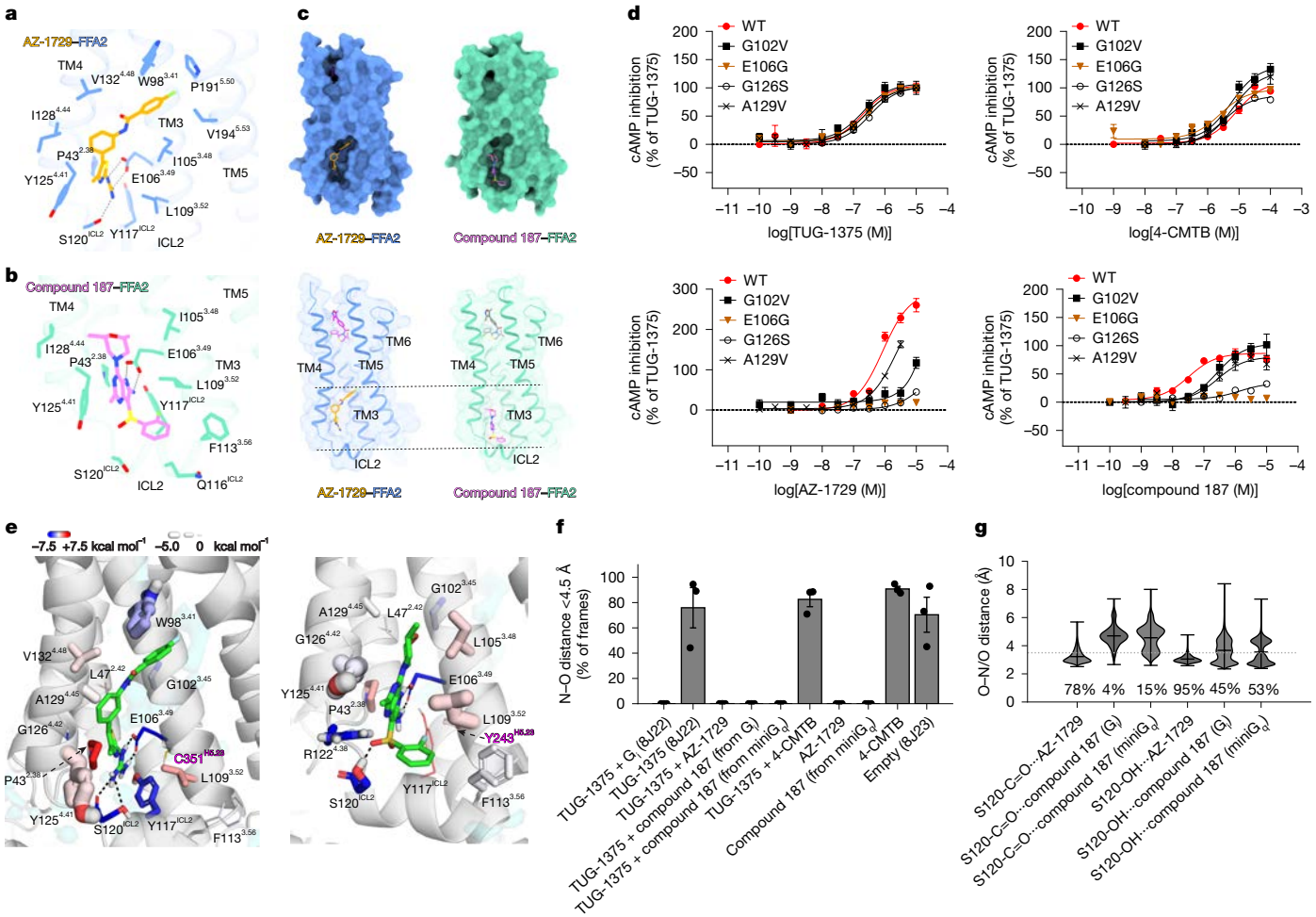

Fig. 4 | Binding of AZ-1729 and compound 187 at site 2. a,**b**, Receptor interaction profiles of AZ-1729 (**a**) and compound 187 (**b**) in the upper and lower regions, respectively, of site 2. **c**, Different binding modes of AZ-1729 and compound 187. The area of each pocket was calculated using PyMol. **d**, Effects of mutations in site 2 on the function of FFA2 ligands measured by cAMP inhibition. Although these mutations affect the function of AZ-1729 and compound 187, they have little effect on the function of TUG-1375 and 4-CMTB. Data are the mean ± s.e.m. $n = 3$ (3 biologically independent experiments). **e**, Simulation snapshots of AZ-1729 (left) and compound 187 (right) bound to FFA2. Protein residues are shown with carbon colours and stick thickness denoting the simulation-averaged energies of electrostatic and van der Waals interactions of each residue with the ligand, respectively. Transparent iso-surfaces illustrate water presence in >50% of the simulation trajectory. Hydrogen bonds are shown with dotted lines. **f**, Distances between the E106$^{3.49}$ side-chain oxygens and R107$^{3.50}$ showing the disruption of their contact only in the presence of a G protein, AZ-1729 or compound 187 (mean ± s.e.m., $n = 3$ (3× 1-µs simulations)). **g**, Distribution of distances between the backbone and side-chain oxygen of S120^{ICL2} and the donor nitrogen of AZ-1729 or the acceptor hydrogens of compound 187. Violin plots show probability densities from three simulation replicates per complex. Horizontal bars indicate minimum, maximum and median values. The dotted line at 3.5 Å shows the hydrogen-bond distance cut-off. Percentages indicate the proportion of frames with distances ≤3.5 Å.

reduction in potency for this ligand than for AZ-1729 (Extended Data Table 2c). Notably, alteration of L109$^{3.52}$ to either alanine or valine resulted in a large reduction in potency for compound 187 (Extended Data Table 2c and Extended Data Fig. 4e).

The cryo-EM structures and MD simulations revealed key differences in how compound 187 and AZ-1729 interact with FFA2 (Fig. 4e). The fluorophenyl ring of AZ-1729 extends to form T-shaped aromatic interactions with W98$^{3.41}$, whereas compound 187 adopts a more compact conformation and is positioned closer to ICL2, thereby precluding such interactions (Fig. 4a–c). Unlike AZ-1729, compound 187 lacks a positively charged group near S120^{ICL2} but features a bulky hydrogen-bond acceptor, which resulted in distinct effects on the conformation of ICL2 (Fig. 4e). MD simulations demonstrated that AZ-1729 establishes a dynamic hydrogen-bond network with both the backbone carbonyl and side-chain hydroxyl of S120^{ICL2}, unlike compound 187 (Fig. 4e,g). However, S120^{ICL2}E showed a modest effect on AZ-1729 only, and S120^{ICL2}F had no effect on the activity of either of the ago-PAMs, which suggested that the S120^{ICL2} side chain has a minimal role in ligand function (Extended Data Table 2c). Conversely, residues involved in G protein interactions had a greater impact on function (Extended Data Fig. 5a–c). Y117^{ICL2}A substantially reduced the potency for both compound 187 (100-fold) and AZ-1729 (50-fold), with modest effects on 4-CMTB and TUG-1375 (Extended Data Table 2c). As Y117^{ICL2}F did not show significant effects on potency (Extended Data Table 2b,c), aromaticity and/or hydrophobic contacts at Y117^{ICL2} are therefore crucial for site 2 PAM activity. R121^{ICL2}A moderately decreased the potency of all compounds, with the greatest effect on AZ-1729, whereas Q116^{ICL2}A had no significant effect (Extended Data Table 2c). Owing to its proximity to ICL2, the 2-fluorophenyl moiety of compound 187 forms extensive backbone contacts and a T-shaped aromatic interaction with F113$^{3.56}$, which were not observed for AZ-1729 (Fig. 4a,b,e). Together with the aromatic contacts of the 5,7-diazaindole fragment with Y125$^{5.41}$ (Fig. 4b,e), these interactions establish the binding of compound 187 at both sides of ICL2. The observed binding mode retrospectively explains the available SAR data for compound 187 (ref. 44) and demonstrates the importance of the 2-aminopyrrole present in compound 187. That is, analogues that

lack this group have half maximal effective concentration (EC_{50}) values of >5 μM. By contrast, variations in the sulfone group, morpholine fragment and the pyrimidine part of the scaffold did not significantly decrease potency, a result in agreement with the lack of specific polar interactions between these regions and the receptor.

FFA2 allosteric activation and modulation

On the basis of structural analyses of the C4–FFA2–miniG_q complex, we previously proposed that the interactions between the carboxylate group of C4 with R180$^{5.39}$ and R255$^{7.35}$ of FFA2 cause inward movements of TM5 and TM7 and concomitant conformational changes of the P191$^{5.50}$T97$^{3.40}$F231$^{6.44}$ motif. This structural change in turn leads to the outward movement of TM6 at the cytoplasmic region, a hallmark of GPCR activation[21]. A similar mechanism may also apply to TUG-1375, which forms similar interactions with R180$^{5.39}$ and R255$^{7.35}$ at the orthosteric binding pocket (Extended Data Fig. 3a). This canonical activation mechanism that involves conformational changes of the P$^{5.50}$I$^{3.40}$F$^{6.44}$ triad motif at the core region of the transmembrane helical bundle has been observed across many other class A GPCRs[5,45,46].

To understand the distinct activation mechanisms of FFA2 ago-PAMs, we conducted MD simulations to examine conformational changes after the removal of an ago-PAM and in PAM-only conditions using various FFA2 cryo-EM structures and docked structures. AZ-1729 and compound 187 form strong electrostatic interactions with E106$^{3.49}$ of the conserved (D/E)R$^{3.50}$Y motif$^{5.47}$ in site 2 (Fig. 4a,b,e). These disrupt the inactive-state intramotif E106$^{3.49}$–R107$^{3.50}$ interaction[5,43,45,47], which remains stable in the empty receptor form and in TUG-1375-only simulations (Fig. 4f). Analyses of additional molecular switches showed that the interhelical R107$^{3.50}$–Y199$^{5.58}$ interaction, which is highly stable in the G-protein-bound state, is also stabilized by AZ-1729 and compound 187 in G-protein-free simulations compared with TUG-1375 alone (Extended Data Fig. 5d). Similarly, R107$^{3.50}$ positioning near the NP$^{7.50}$XXY motif (where X denotes any amino acid), crucial for G protein coupling, is strongly maintained by AZ-1729 and compound 187 but is less stable with TUG-1375 alone or in empty-receptor simulations (Extended Data Fig. 5e). These findings, together with our pharmacology and cooperativity studies, demonstrate that AZ-1729 and compound 187 act as allosteric agonists by promoting active-state conformations and function as PAMs by enhancing TUG-1375-induced receptor activation.

ICL2 is another important region involved in the action of site 2 PAMs. Both AZ-1729 and compound 187 form multiple interactions with ICL2 residues to stabilize its backbone conformation. Studies of FFA1 (also known as GPR40)[48–50] have shown that ago-PAMs that bind above ICL2 stabilize a specific ICL2 conformation that makes G-protein-coupling more effective. Similarly, the site 2 ago-PAMs of FFA2 substantially reduce the flexibility of ICL2 and increase its stability in our simulations compared with those in the absence of ago-PAMs (Fig. 5a and Extended Data Fig. 5f–k). By contrast, 4-CMTB, which binds away from ICL2, had little impact on ICL2 dynamics (Fig. 5a and Extended Data Fig. 5f–k). The effects of AZ-1729 and compound 187 on ICL2 persisted across different structural contexts, with the effects of compound 187 being more dependent on G protein binding (Extended Data Fig. 5f–k).

For 4-CMTB, our MD simulations revealed its impacts on a hydrogen-bond network mediated by N230$^{6.43}$ at the TM6–TM7 interface. In simulations with 4-CMTB alone and docked to TUG-1375-bound FFA2, 4-CMTB disrupts the N230$^{6.43}$–D269$^{7.49}$ polar contact at the TM6–TM7 interface by forming stable interactions with N230$^{6.43}$ (Fig. 5b). This disruption affects a broader hydrogen-bond network that involves N265$^{7.45}$, C234$^{6.47}$ and D55$^{2.50}$, which in turn affects the conserved (N/D)$^{7.49}$P$^{7.50}$XXY and C$^{6.47}$W$^{6.48}$XP$^{6.50}$ motifs as well as the sodium-coordination pocket, all of which are crucial for GPCR activation[5,46] (Extended Data Fig. 5l,m). Accordingly, after the removal of 4-CMTB, N230$^{6.43}$ rotates towards TM7 to re-establish an extensive hydrogen-bond network with N265$^{7.45}$, D269$^{7.49}$ and C234$^{6.47}$ (Fig. 5c and Extended Data Fig. 5l,m). This network seems to constrain TM6 movement, as TM6–TM7 hydrogen bonds are more frequent in unliganded, G-protein-free simulations of FFA2 compared with FFA2 complexes with agonists, especially 4-CMTB (Extended Data Fig. 5n). Moreover, MD simulations of N230$^{6.43}$D and N230$^{6.43}$A mutants showed that N230A mimics the effect of 4-CMTB by disrupting the cytoplasmic TM6–TM7 hydrogen-bond network, whereas N230D can reverse such an effect (Extended Data Fig. 5n).

Mechanism of FFA2 biased signalling

Despite the apparently similar receptor activation mechanism for AZ-1729 and compound 187, which involves the stabilization of ICL2, they displayed divergent G protein selectivity. That is, AZ-1729 is unable to effectively activate G_q but exhibits markedly higher G_i efficacy compared with compound 187, as measured in cAMP-inhibition assays[19] (Fig. 1d). Such functional selectivity or a biased signalling property of AZ-1729 for G_i over G_q is not commonly seen for GPCR allosteric modulators[51].

The G_i-coupled and miniG_q-coupled FFA2 complex structures showed high overall similarity. FFA2 forms comparable interaction patterns with both G proteins (Extended Data Fig. 6a,b). Despite these structural similarities, subtle conformational differences were observed when comparing FFA2–G_i and FFA2–miniG_q interfaces, including different orientations of the αN helix of G_i and miniG_q (Extended Data Fig. 6c). Moreover, R217$^{6.30}$ and Q215$^{6.28}$ engage in polar interactions with the α5 helix of miniG_q, which are missing in the G_i-coupled FFA2 structures (Extended Data Fig. 6d). Notably, as m$G\alpha_{i/s/q}$ is a chimeric protein derived from mini$G\alpha_s$, $G\alpha_q$ and $G\alpha_i$, interactions beyond the last 15 amino acids of the α5 helix and the amino-terminal αN helix reflect G_s interactions, which may not accurately represent native G_q–receptor interactions. Our cryo-EM structures and MD simulations showed that AZ-1729 and compound 187 stabilize distinct helical conformations of ICL2 (Figs. 5a and 6a). Specifically, interactions of AZ-1729 with S120^{ICL2} significantly alter the ICL2 backbone conformation, reorienting it towards the membrane plane (Figs. 4e,g and 5a). As a result, there is an internal rotation and an upwards shift of ICL2 in FFA2 bound to AZ-1729 compared with that in FFA2 bound to compound 187 (Fig. 6a). Such a S120^{ICL2} interaction is not possible for compound 187 owing to the hydrogen-bond acceptor nature of its sulfonamide group (Fig. 4e,g). This distinct ICL2 conformation was observed in simulations of all AZ-1729-containing complexes regardless of the presence of a G protein (Fig. 6b).

Our MD simulations further revealed contrasting G protein effects on ICL2 of FFA2. Although miniG_q-bound FFA2 showed similar ICL2 conformations across all ligands (Fig. 5a), G_i-bound FFA2 displayed ligand-dependent ICL2 conformations (Fig. 5a). Notably, the ICL2 conformation in the G_i–compound 187–FFA2 complex closely resembled that observed in G-protein-free simulations (Figs. 5a and 6b), whereas ICL2 conformations markedly differed between miniG_q-bound and G_q-free simulations. This result suggests that G_i coupling facilitates greater ICL2 flexibility compared with miniG_q coupling. Given the critical role of ICL2 in G protein coupling[50], we propose that AZ-1729 stabilizes a specific ICL2 conformation that favours productive coupling with G_i over G_q.

Although the specific interactions that drive this biased property of AZ-1729 are not immediately apparent, mutagenesis and MD simulation studies provided mechanistic insights. The α5 helix (or helix 5) of the Gα subunit has an important role in determining G-protein-coupling specificity[52,53]. In the FFA2–miniG_q structure, the part of α5 helix of m$G\alpha_{i/s/q}$ at the receptor-coupling interface is the same as that of the wild-type $G\alpha_q$ protein, in which the sequence variations between G_i and G_q are preserved. Among these residues, C351$^{H5.23}$ (G protein residue numbering[54]) in G_i, the site of pertussis-toxin-catalysed ADP-ribosylation

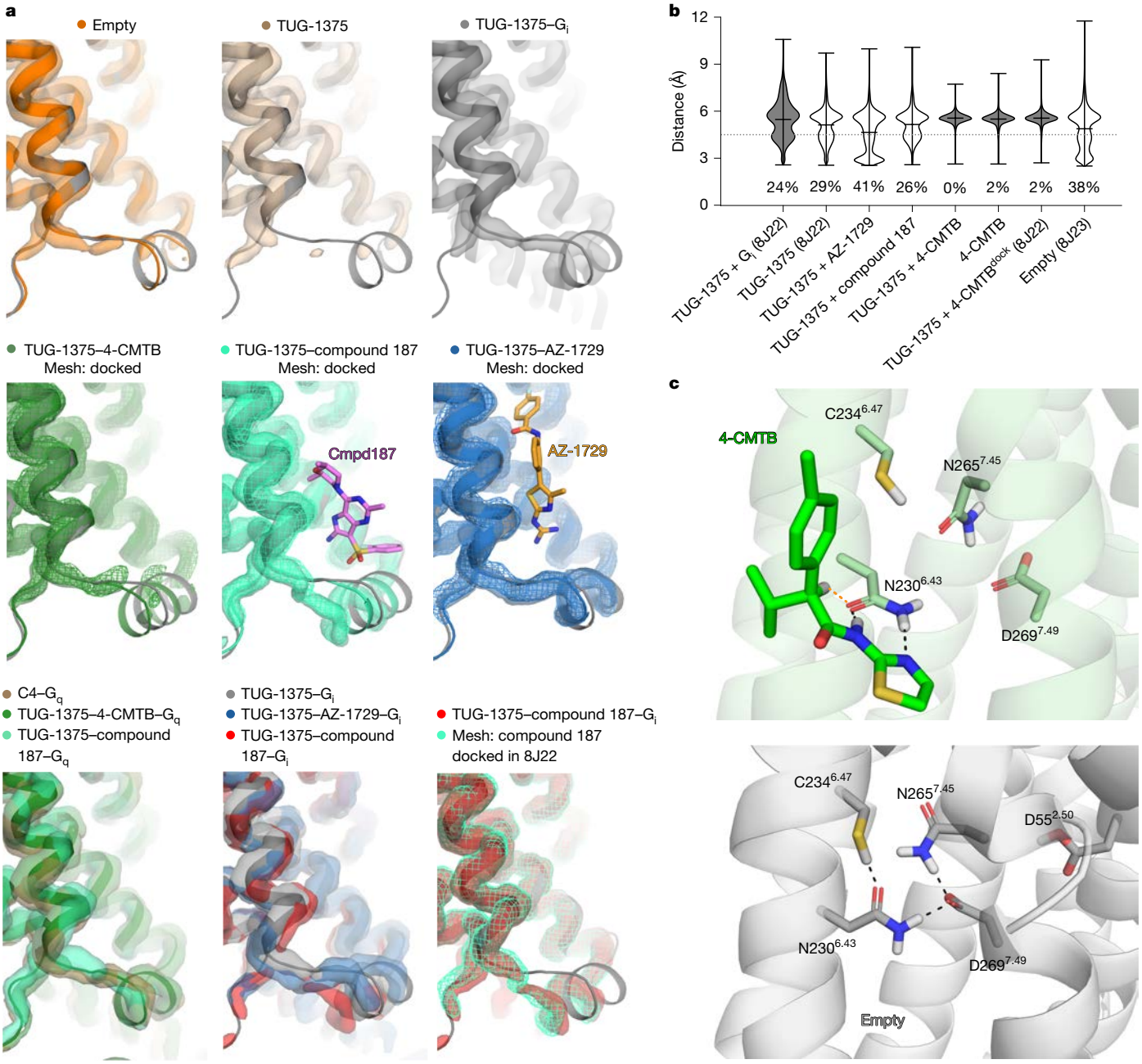

Fig. 5 | Noncanonical FFA2 activation mechanisms revealed by MD simulations. a, Cartoons showing cryo-EM structures of FFA2–TUG-1375–G_i (PDB accession 8J22; grey), FFA2–4-CMTB–miniG_q (dark green), FFA2–compound 187–miniG_q (cyan) and FFA2–AZ-1729–G_i (blue) overlaid with surfaces representing FFA2 main chain atoms occupied at >75% of simulation time. Solid surfaces show cryo-EM-based simulations; meshes show docking-based simulations to structure 8J22. Top row, empty FFA2 (PDB accession 8J23; orange), FFA2–TUG-1375 (beige) and FFA2–TUG-1375–G_i (8J22; grey) demonstrate G protein but not orthosteric ligand stabilization of ICL2. Middle row, G-protein-free simulations with 4-CMTB (dark green), compound 187 (Cmpd187) (cyan) and AZ-1729 (blue) show ICL2 stabilization by AZ-1729 and compound 187, with compound 187 causing deviation of ICL2 from the cryo-EM structure. Bottom left, miniG_q-bound simulations with C4 (PDB accession 8T3S; olive), TUG-1375–4-CMTB (dark green) and TUG-1375–compound 187 (cyan), showing similar ICL2 conformations. Bottom middle, comparison of G_i-bound FFA2–TUG-1375 (grey) with FFA2–TUG-1375–AZ-1729 (blue) and FFA2–TUG-1375–compound 187 (red), revealing distinct ICL2 conformations compatible with G_i coupling. Bottom right, contrast of G_i-bound and G-protein-free simulations of FFA2–compound 187, showing the minimal impact of G_i binding on compound 187-induced ICL2 conformation. **b**, Distribution of distances between $N230^{6.43}$ side-chain nitrogen ($N^{\delta2}$) and $D269^{7.49}$ carboxyl oxygens ($O^{\delta1,\delta2}$) across simulated complexes. Labels in parentheses indicate PDB accession numbers of the complexes. Violin plots show probability densities from three simulation replicates per complex. Horizontal bars indicate minimum, maximum and median values. The dotted line at 4.5 Å shows the interaction distance cut-off. Percentages indicate the proportion of frames with distances ≤4.5 Å. **c**, Snapshots of site 1 from MD simulations with 4-CMTB (top) and without (bottom), highlighting hydrogen bonds (dashed lines) among $N230^{6.43}$, $C234^{6.47}$, $N265^{7.45}$ and $D269^{7.49}$ residues critical for allosteric modulation.

that prevents GPCR–G_i coupling, is replaced by a considerably bulkier $Y243^{H5.23}$ in mG$\alpha_{i/s/q}$ ($Y356^{H5.23}$ in wild-type $G_{\alpha q}$) (Fig. 6a). Both of these G protein residues extend towards ICL2 of FFA2 in our cryo-EM structures (Fig. 6a). Our MD simulations revealed that the distance between $Y117^{ICL2}$ of AZ-1729-bound FFA2 and $C351^{H5.23}$ of G_i is shorter than the distance between $Y117^{ICL2}$ of FFA2 bound to either 4-CMTB or

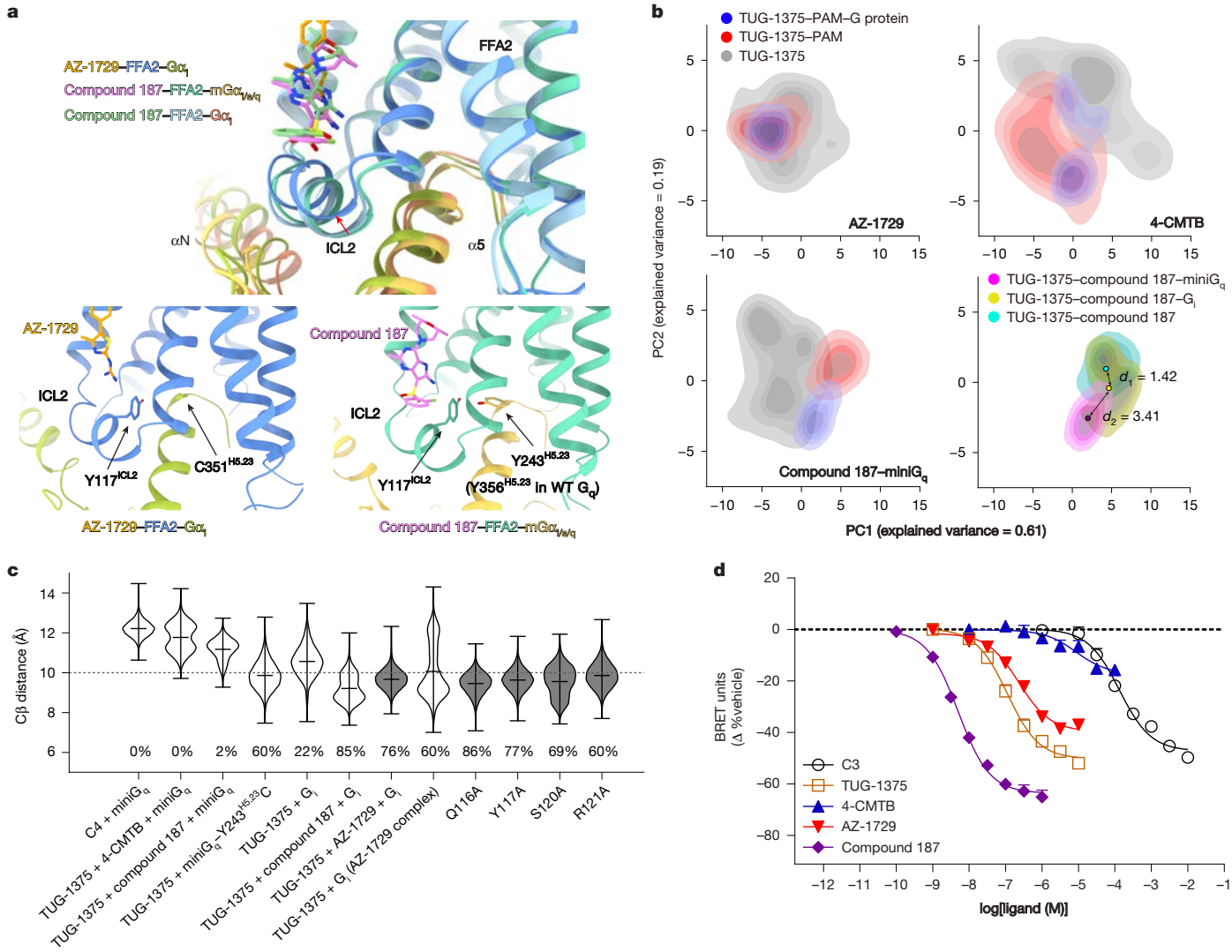

Fig. 6 | Distinct ICL2 conformations induced by AZ-1729 and compound 187 confer differential G-protein-subtype selectivity. a, ICL2 conformations in FFA2–G_i complexes with AZ-1729 (orange) and compound 187 (light green), and FFA2–miniG_q complex with compound 187 (pink). Gα5 helices are coloured for $Gα_i$ with AZ-1729 (green-yellow), $Gα_i$ with compound 187 (light orange) and $mGα_{q/s/i}$ (dark yellow). The red arrow indicates the uplifted ICL2 conformation with AZ-1729. $Y117^{ICL2}$ faces $C351^{H5.23}$ of $Gα_i$ or $Y243^{H5.23}$ of $mGα_{q/s/i}$ ($Y356^{H5.23}$ in wild-type $Gα_q$). **b**, Kernel density plots in two dimensional principal component analysis (2D-PCA) of ICL2 (P114–R121) Cα atoms for select simulations, with colours showing the iso-proportion density from 20%. Top left, FFA2–TUG-1375–AZ-1729–G_i (blue), FFA2–TUG-1375–AZ-1729 without G protein (red) and FFA2–TUG-1375 alone (grey). Top right, similar simulations for FFA2–TUG-1375–4-CMTB–miniG_q. Bottom left, simulations for FFA2–TUG-1375–compound 187–miniG_q. Bottom right, FFA2–TUG-1375–compound 187–miniG_q (purple), FFA2–TUG-1375–compound 187–G_i (yellow) and FFA2–TUG-1375–compound 187 without G protein (cyan). Coloured dots show simulation-average ICL2 positions; distances d_1 and d_2 connect the G_i-bound simulation to G-protein-free and miniG_q-bound states, respectively. ICL2 conformations show greater similarity between G_i-bound and G-protein-free states ($d_1 = 1.42$) than with G_q-bound states ($d_2 = 3.41$). **c**, Distribution of Cβ atom distances between $Y117^{ICL2}$ and $Y243^{H5.23}$ ($mGα_{q/s/i}$) or $C351^{H5.23}$ ($Gα_i$) across simulated complexes. Violin plots show probability densities from three simulation replicates per complex. Horizontal bars indicate minimum, maximum and median values. The dotted line at 10 Å shows the interaction distance cut-off. Percentages indicate the proportion of frames with distances ≤10 Å. **d**, TRUPATH assays using the G_q $Y356^{H5.23}C$ sensor (Y243H5.23 in $mGα_{q/s/i}$) and wild-type FFA2, showing the potency and efficacy of indicated ligands. Data are the mean ± s.e.m. $n = 3$ (3 biologically independent experiments).

compound 187 and $Y243^{H5.23}$ of $mGα_{i/s/q}$ (Fig. 6c). Furthermore, in our MD simulations, replacing $Y243^{H5.23}$ in miniG_q with cysteine shifts its positioning to resemble that in G_i relative to $Y117^{ICL2}$ of FFA2, whereas AZ-1729 promotes a closer positioning of $C351^{H5.23}$ of G_i to $Y117^{ICL2}$ (Fig. 6c).

All of the above results suggest that the conformation of $Y117^{ICL2}$ in the AZ-1729-bound FFA2 is incompatible with coupling to G_q owing to a potential steric clash with $Y356^{H5.23}$. We therefore proposed that replacing $Y356^{H5.23}$ of G_q with a less bulky C351 as in G_i would enable its coupling to AZ-1729-bound FFA2. Data from TRUPATH assays confirmed that AZ-1729 effectively activated the Y356C G_q mutant (Fig. 6d) while showing minimal activation of the wild-type G_q (Fig. 1c). Notably, activation of the Y356C G_q variant by compound 187 and the orthosteric agonists C3 and TUG-1375 was as effective as for the wild-type G_q (Fig. 6d). These results suggest that the specific ICL2 conformation induced by AZ-1729 preferentially favours receptor coupling to G_i with its $C351^{H5.23}$ residue in the α5 helix over G_q, which has the bulkier $Y356^{H5.23}$. It is also interesting to note that $C351^{H5.23}$ in G_i isoforms can be replaced by a broad range of other amino acids, with receptor coupling efficiency largely correlated with residue hydrophobicity[55]. By contrast, 4-CMTB exhibited similarly weak activity on the Y356C G_q variant as it does on the wild-type G_q (Figs. 1c and 6d), which suggests that ICL2 is not involved in the G protein selectivity of this compound.

Discussion

Our structural and pharmacological studies revealed that the three ago-PAMs 4-CMTB, AZ-1729 and compound 187 bind to distinct allosteric sites and use noncanonical mechanisms to activate FFA2, a result that highlights the complex and diverse modes of allosteric modulation of FFA2. Despite this binding diversity, all three allosteric agonists exhibited similar cooperativity effects with the synthetic agonist TUG-1375 and the SCFA C3 (Extended Data Fig. 1c), which suggests that there is limited 'probe-dependence' and conserved communication pathways between the allosteric pockets and orthosteric ligands. Our pharmacological studies also demonstrated cooperative effects between AZ-1729 or compound 187 and 4-CMTB (Fig. 2b). Consistent with this finding, compound 3, an initial member of the Takeda series chemically similar to compound 187, also showed positive cooperative effects with both C3 and 4-CMTB (Extended Data Fig. 7a). Furthermore, our findings indicate that ICL2 can adopt multiple conformations, functioning as a crucial determinant for both receptor activation and biased G protein coupling. These insights advance our understanding of GPCR allosteric modulation and provide a foundation for the rational design of new FFA2-targeting therapeutics for metabolic diseases.

Diverse allosteric sites in FFA2 and noncanonical activation mechanisms

GPCRs exhibit high conformational dynamics and sample multiple states even when bound to antagonists or agonists[56,57]. Several conserved structural motifs or macroswitches and microswitches play important parts in receptor activation[5,46]. Orthosteric agonists and allosteric activators can differentially engage these structural elements to modulate GPCR conformational equilibria. Our studies of FFA2 suggest that diverse allosteric modulators engage distinct sets of conserved motifs, which lead to receptor activation through different noncanonical mechanisms.

Our pharmacological and structural studies confirmed two distinct allosteric sites, site 1 and site 2, in FFA2, both located at the interface between the seven transmembrane bundle of the receptor and the membrane bilayer. Site 1 for 4-CMTB is flat and superficial compared with site 2. This type of allosteric site is uncommon among class A GPCRs. To our knowledge, a similar site has only been observed for the A_1R PAM MIPS521 (ref. 38) (Fig. 3a). However, MIPS521 binds closer to TM7 and TM1 of A_1R to form interactions with all three helices, whereas 4-CMTB interacts primarily with TM6 of FFA2. Nevertheless, MIPS521 has been suggested to facilitate the 'G-protein-bound-like' conformation of TM6 and TM7 (ref. 38), a result that aligns with our proposed noncanonical receptor activation mechanism for 4-CMTB. This mechanism involves the disruption of the interhelical hydrogen-bond network through effects on the $(N/D)^{7.49}P^{7.50}XXY$ and the $C^{6.47}W^{6.48}XP^{6.50}$ motifs to promote and stabilize an 'active-like' conformation of TM6.

By contrast, site 2 in FFA2 for AZ-1729 and compound 187, located above ICL2, represents a more common allosteric pocket in class A GPCRs. Similar sites exist in FFA1, the dopamine D_1 receptor and the β_2-adrenergic receptor[48,58,59]. However, this site in FFA2 has distinct residue compositions and structural features compared with other free fatty acid receptors, thereby providing receptor selectivity for PAMs that target this site. Indeed, both AZ-1729 and compound 187 do not act on other free fatty acid receptors, which may be due to potential steric clash (Extended Data Fig. 7b).

Our MD simulations suggested that AZ-1729 and compound 187 at site 2 can directly interact with the conserved D/ERY motif and influence its conformation to promote G protein coupling and receptor activation. This mechanism has not been reported for PAMs that target similar sites in other GPCRs. ICL2 serves as another critical structural element in site-2-mediated receptor activation[50]. Previous studies have shown that FFA1 PAMs interact with ICL2 to stabilize a helical conformation that makes the receptor couple to G proteins more effectively[48–50]. Consistently, our MD simulations of FFA2 revealed increased ICL2 flexibility in the absence of AZ-1729 and compound 187. Therefore, we propose that AZ-1729 and compound 187 not only modulate the D/ERY motif but also induce ligand-specific conformational changes in ICL2 to facilitate G protein coupling.

So far, similar ICL2-proximate allosteric sites have not been identified for FFA3 or FFA4. Nevertheless, for FFA3, a recent study[22] showed that the PAM AR420626 binds to an intrahelical allosteric site immediately above the coupled G_i protein to form direct interactions with G_i. For FFA4, to our knowledge, no synthetic PAMs have been identified thus far. Notably, our previous structures[21] revealed that the ICL2 in FFA4 is disordered even when coupled to miniG_q, which suggests that a well-structured ICL2 is not required for the activation of FFA4. Therefore, it might not be feasible to identify or develop FFA4 PAMs similar to AZ-1729 or compound 187 for FFA2, which function by stabilizing specific conformations of ICL2. The identification of FFA4 PAMs represents a highly challenging task.

ICL2 in FFA2 activation, biased signalling and beyond

Our previous structural studies of another GPCR, the C5a receptor (C5aR), identified an allosteric site above ICL2 for negative allosteric modulators (NAMs) or allosteric antagonists[60]. In that study[60], we also identified this site as a hot spot for lipid binding in numerous class A GPCRs. The concave shape of this site, along with a mix of hydrophobic residues from transmembrane helices and hydrophilic residues from ICL2, may make it an ideal binding site for lipids and allosteric modulators. This allosteric site in C5aR partially overlaps with site 2 in FFA2. Notably, C5aR NAMs do not directly interact with ICL2, even though ICL2 adopts a helical conformation in the crystal structures of inactive C5aR bound to NAMs[60] (Extended Data Fig. 7c). This finding indicates that direct interactions with ICL2 may be important for the positive allosteric action of site 2 PAMs of FFA2.

Our current results further revealed that subtle conformational variations in ICL2 can lead to selective or biased signalling towards specific G protein subtypes. We demonstrated that the $Y117^{ICL2}$–$Y356G_q$–α5 clash is responsible for the G protein activation bias exhibited by AZ-1729. In addition to G proteins, ICL2 can affect β-arrestin binding and activation[50,61]. Our pharmacological studies showed that compound 187 is a G-protein-biased ago-PAM that has no detectable activity in β-arrestin 2 recruitment assays (Fig. 1d). However, the molecular mechanism that underlies this biased signalling is currently unclear. We did not observe apparent structural differences between FFA2 bound to compound 187 and 4-CMTB, despite the latter being capable of inducing arrestin recruitment (Fig. 1d). It may be that compound 187 induces specific conformational dynamics in the cytoplasmic region of FFA2, including ICL2, thereby affecting arrestin coupling. Nevertheless, in line with previous MD simulations studies of FFA1 PAMs[50], our results imply that the development of GPCR PAMs that target ICL2-proximate allosteric sites with selective or biased signalling profiles represents a feasible strategy for many class A GPCRs. A deeper understanding of how different ICL2 conformations confer distinct preferences of a given GPCR for diverse signalling partners will aid in the rational design of such biased GPCR PAMs, which could offer new opportunities in drug development.

Online content

Any methods, additional references, Nature Portfolio reporting summaries, source data, extended data, supplementary information, acknowledgements, peer review information; details of author contributions and competing interests; and statements of data and code availability are available at https://doi.org/10.1038/s41586-025-09186-6.

1. Stoddart, L. A., Smith, N. J. & Milligan, G. International Union of Pharmacology. LXXI. Free fatty acid receptors FFA1, -2, and -3: pharmacology and pathophysiological functions. *Pharmacol. Rev.* **60**, 405–417 (2008).

2. Alvarez-Curto, E. & Milligan, G. Metabolism meets immunity: the role of free fatty acid receptors in the immune system. *Biochem. Pharmacol.* **114**, 3–13 (2016).
3. Kimura, I., Ichimura, A., Ohue-Kitano, R. & Igarashi, M. Free fatty acid receptors in health and disease. *Physiol. Rev.* **100**, 171–210 (2020).
4. McCarville, J. L., Chen, G. Y., Cuevas, V. D., Troha, K. & Ayres, J. S. Microbiota metabolites in health and disease. *Annu. Rev. Immunol.* **38**, 147–170 (2020).
5. Zhou, Q. et al. Common activation mechanism of class A GPCRs. *eLife* **8**, e50279 (2019).
6. Milligan, G., Shimpukade, B., Ulven, T. & Hudson, B. D. Complex pharmacology of free fatty acid receptors. *Chem. Rev.* **117**, 67–110 (2017).
7. Maslowski, K. M. et al. Regulation of inflammatory responses by gut microbiota and chemoattractant receptor GPR43. *Nature* **461**, 1282–1286 (2009).
8. Kimura, I. et al. The gut microbiota suppresses insulin-mediated fat accumulation via the short-chain fatty acid receptor GPR43. *Nat. Commun.* **4**, 1829 (2013).
9. Zhao, Y. et al. GPR43 mediates microbiota metabolite SCFA regulation of antimicrobial peptide expression in intestinal epithelial cells via activation of mTOR and STAT3. *Mucosal Immunol.* **11**, 752–762 (2018).
10. Antunes, K. H. et al. Microbiota-derived acetate protects against respiratory syncytial virus infection through a GPR43-type 1 interferon response. *Nat. Commun.* **10**, 3273 (2019).
11. Kimura, I., Inoue, D., Hirano, K. & Tsujimoto, G. The SCFA receptor GPR43 and energy metabolism. *Front. Endocrinol.* **5**, 85 (2014).
12. Bindels, L. B., Dewulf, E. M. & Delzenne, N. M. GPR43/FFA2: physiopathological relevance and therapeutic prospects. *Trends Pharmacol. Sci.* **34**, 226–232 (2013).
13. Huang, S. et al. Lithium carbonate alleviates colon inflammation through modulating gut microbiota and T_{reg} cells in a GPR43-dependent manner. *Pharmacol. Res.* **175**, 105992 (2022).
14. Park, B. O. et al. Novel GPR43 agonists exert an anti-Inflammatory effect in a colitis model. *Biomol. Ther.* **30**, 48–54 (2022).
15. Hansen, A. H. et al. Discovery of a potent thiazolidine free fatty acid receptor 2 agonist with favorable pharmacokinetic properties. *J. Med. Chem.* **61**, 9534–9550 (2018).
16. Lee, T. et al. Identification and functional characterization of allosteric agonists for the G protein-coupled receptor FFA2. *Mol. Pharmacol.* **74**, 1599–1609 (2008).
17. Smith, N. J. et al. Extracellular loop 2 of the free fatty acid receptor 2 mediates allosterism of a phenylacetamide ago-allosteric modulator. *Mol. Pharmacol.* **80**, 163–173 (2011).
18. Milligan, G., Bolognini, D. & Sergeev, E. in *Free Fatty Acid Receptors* (eds Milligan, G. & Kimura, I) 17–32 (Springer, 2017).
19. Bolognini, D. et al. A novel allosteric activator of free fatty acid 2 receptor displays unique G_i-functional bias. *J. Biol. Chem.* **291**, 18915–18931 (2016).
20. Park, B. O. et al. The short-chain fatty acid receptor GPR43 modulates YAP/TAZ via RhoA. *Mol. Cells* **44**, 458–467 (2021).
21. Zhang, X. et al. Structural basis for the ligand recognition and signaling of free fatty acid receptors. *Sci. Adv.* **10**, eadj2384 (2024).
22. Li, F. et al. Molecular recognition and activation mechanism of short-chain fatty acid receptors FFAR2/3. *Cell Res.* **34**, 323–326 (2024).
23. Brown, A. J. et al. The orphan G protein-coupled receptors GPR41 and GPR43 are activated by propionate and other short chain carboxylic acids. *J. Biol. Chem.* **278**, 11312–11319 (2003).
24. Hudson, B. D. et al. Chemically engineering ligand selectivity at the free fatty acid receptor 2 based on pharmacological variation between species orthologs. *FASEB J.* **26**, 4951–4965 (2012).
25. Wang, Y. et al. The first synthetic agonists of FFA2: discovery and SAR of phenylacetamides as allosteric modulators. *Bioorg. Med. Chem. Lett.* **20**, 493–498 (2010).
26. Lind, S. et al. Interdependent allosteric free fatty acid receptor 2 modulators synergistically induce functional selective activation and desensitization in neutrophils. *Biochim. Biophys. Acta Mol. Cell. Res.* **1867**, 118689 (2020).
27. Olsen, R. H. J. et al. TRUPATH, an open-source biosensor platform for interrogating the GPCR transducerome. *Nat. Chem. Biol.* **16**, 841–849 (2020).
28. Sergeev, E. et al. Non-equivalence of key positively charged residues of the free fatty acid 2 receptor in the recognition and function of agonist versus antagonist ligands. *J. Biol. Chem.* **291**, 303–317 (2016).
29. Kim, K. et al. Structure of a hallucinogen-activated G_q-coupled 5-HT_{2A} serotonin receptor. *Cell* **182**, 1574–1588 (2020).
30. Xia, R. et al. Cryo-EM structure of the human histamine H_1 receptor/G_q complex. *Nat. Commun.* **12**, 2086 (2021).
31. Meyerowitz, J. G. et al. The oxytocin signaling complex reveals a molecular switch for cation dependence. *Nat. Struct. Mol. Biol.* **29**, 274–281 (2022).
32. Nehme, R. et al. Mini-G proteins: novel tools for studying GPCRs in their active conformation. *PLoS ONE* **12**, e0175642 (2017).
33. Wan, Q. et al. Mini G protein probes for active G protein-coupled receptors (GPCRs) in live cells. *J. Biol. Chem.* **293**, 7466–7473 (2018).
34. Duan, J. et al. Cryo-EM structure of an activated VIP1 receptor–G protein complex revealed by a NanoBiT tethering strategy. *Nat. Commun.* **11**, 4121 (2020).
35. Koehl, A. et al. Structure of the μ-opioid receptor–G_i protein complex. *Nature* **558**, 547–552 (2018).
36. Swaminath, G. et al. Mutational analysis of G-protein coupled receptor—FFA2. *Biochem. Biophys. Res. Commun.* **405**, 122–127 (2011).
37. Grundmann, M. et al. A molecular mechanism for sequential activation of a G protein-coupled receptor. *Cell Chem. Biol.* **23**, 392–403 (2016).
38. Draper-Joyce, C. J. et al. Positive allosteric mechanisms of adenosine A_1 receptor-mediated analgesia. *Nature* **597**, 571–576 (2021).
39. Ballesteros, J. A. & Weinstein, H. in *Methods in Neurosciences* Vol. 25 (ed. Sealfon, S. C.) 366–428 (Academic Press, 1995).
40. Wang, Y., Yu, Z., Xiao, W., Lu, S. & Zhang, J. Allosteric binding sites at the receptor–lipid bilayer interface: novel targets for GPCR drug discovery. *Drug Discov. Today* **26**, 690–703 (2021).
41. Ding, T., Karlov, D. S., Pino-Angeles, A. & Tikhonova, I. G. Intermolecular interactions in G protein-coupled receptor allosteric sites at the membrane interface from molecular dynamics simulations and quantum chemical calculations. *J. Chem. Inf. Model.* **62**, 4736–4747 (2022).
42. Ciancetta, A. et al. Probe confined dynamic mapping for G protein-coupled receptor allosteric site prediction. *ACS Cent. Sci.* **7**, 1847–1862 (2021).
43. Filipek, S. Molecular switches in GPCRs. *Curr. Opin. Struct. Biol.* **55**, 114–120 (2019).
44. Barker, G. et al. 3-Substituted 2-amino-indole derivatives. WIPO patent WO2015/198045 (2015).
45. Weis, W. I. & Kobilka, B. K. The molecular basis of G protein-coupled receptor activation. *Annu. Rev. Biochem.* **87**, 897–919 (2018).
46. Hauser, A. S. et al. GPCR activation mechanisms across classes and macro/microscales. *Nat. Struct. Mol. Biol.* **28**, 879–888 (2021).
47. Manglik, A. & Kruse, A. C. Structural basis for G protein-coupled receptor activation. *Biochemistry* **56**, 5628–5634 (2017).
48. Lu, J. et al. Structural basis for the cooperative allosteric activation of the free fatty acid receptor GPR40. *Nat. Struct. Mol. Biol.* **24**, 570–577 (2017).
49. Ho, J. D. et al. Structural basis for GPR40 allosteric agonism and incretin stimulation. *Nat. Commun.* **9**, 1645 (2018).
50. Powers, A. S. et al. A non-canonical mechanism of GPCR activation. *Nat. Commun.* **15**, 9938 (2024).
51. Slosky, L. M., Caron, M. G. & Barak, L. S. Biased allosteric modulators: new frontiers in GPCR drug discovery. *Trends Pharmacol. Sci.* **42**, 283–299 (2021).
52. Flock, T. et al. Selectivity determinants of GPCR–G-protein binding. *Nature* **545**, 317–322 (2017).
53. Inoue, A. et al. Illuminating G-protein-coupling selectivity of GPCRs. *Cell* **177**, 1933–1947 (2019).
54. Flock, T. et al. Universal allosteric mechanism for Gα activation by GPCRs. *Nature* **524**, 173–179 (2015).
55. Bahia, D. S. et al. Hydrophobicity of residue^{351} of the G protein G_{i1}α determines the extent of activation by the $α_{2A}$-adrenoceptor. *Biochemistry* **37**, 11555–11562 (1998).
56. Manglik, A. & Kobilka, B. The role of protein dynamics in GPCR function: insights from the $β_2$AR and rhodopsin. *Curr. Opin. Cell Biol.* **27**, 136–143 (2014).
57. Hilger, D. The role of structural dynamics in GPCR-mediated signaling. *FEBS J.* **288**, 2461–2489 (2021).
58. Zhuang, Y. et al. Mechanism of dopamine binding and allosteric modulation of the human D_1 dopamine receptor. *Cell Res.* **31**, 593–596 (2021).
59. Liu, X. et al. Mechanism of $β_2$AR regulation by an intracellular positive allosteric modulator. *Science* **364**, 1283–1287 (2019).
60. Liu, H. et al. Orthosteric and allosteric action of the C5a receptor antagonists. *Nat. Struct. Mol. Biol.* **25**, 472–481 (2018).
61. Latorraca, N. R. et al. Molecular mechanism of GPCR-mediated arrestin activation. *Nature* **557**, 452–456 (2018).

Methods

FFA2 ligands

TUG-1375 was from MedChem Express, 4-CMTB, AZ-1729 and CATPB were from Tocris Bioscience, and C3 was from Sigma-Aldrich. [^{3}H] GLPG0974 was produced and characterized in house and has been used in previous studies[28]. Compound 187 was synthesized as detailed in the Supplementary Information.

Protein expression and purification

Human FFA2 was cloned into a pFastBac vector (Thermo Fisher) with the LargeBit subunit fused at the C terminus of the receptor. For the G_q protein, we used $mG\alpha_{i/s/q}$ as the α-subunit as in previous structural studies of other G_q-coupled GPCRs[21,29,30]. $mG\alpha_{i/s/q}$ is based on $miniG\alpha_{q/s}$, which was developed by replacing the C-terminal 15 residues with those of $G\alpha_q$ (refs. 32,33), with the N-terminal 35 amino acids replaced by their corresponding residues from $G\alpha_i$. This chimeric protein retains most of the C-terminal region of the wild-type $G\alpha_q$, which serves as the major interaction interface with the receptor. The $miniG_q$ heterotrimers with this chimera $mG\alpha_{i/s/q}$ as the α-subunit have been successfully used in our previous cryo-EM studies of G_q-coupled FFA1, FFA2 and FFA4 with free fatty acid ligands[21], along with studies of other G_q-coupled GPCRs from other groups[29–31]. The $mG\alpha_{i/s/q}$ subunit was cloned into a pFastBac vector. Human $G\beta_1$ was fused with an N-terminal His_6-tag and a C-terminal HiBiT subunit connected with a 15-amino-acid linker, which was cloned into a pFastBac dual vector (Thermo Fisher) together with human $G\gamma_2$. For the G_i protein, we used a dominant-negative $G\alpha_{i1}$ (ref. 62) as the α-subunit.

ScFv16 was expressed and purified as previously described[21]. In brief, scFv16 was expressed in Tni insect cells and purified from the medium by Ni affinity. scFv16 was further purified by size-exclusion chromatography using a Superdex 200 Increase 100/300 GL column (GE Healthcare) and stored at −80 °C before use.

FFA2, $mG\alpha_{i/s/q}$ or dominant-negative $G\alpha_{i1}$ and $G\beta_1\gamma_2$ were co-expressed in Sf9 insect cells using the Bac-to-Bac method. Cells were infected with 3 types of viruses at a ratio of 1:1:1 for 48 h at 27 °C. After infection, cell pellets were collected by centrifugation and stored at −80 °C before use. Frozen cells were thawed in lysis buffer containing 20 mM HEPES, pH 7.5, 50 mM NaCl, 10 mM $MgCl_2$, 5 mM $CaCl_2$, 2.5 μg ml^{-1} leupeptin and 300 μg ml^{-1} benzamidine. To facilitate the formation of complexes, 10 μM TUG-1375, 10 μM PAMs (4-CMTB, compound 187 or AZ-1729), 25 mU ml^{-1} apyrase (NEB) and 100 μM TCEP were added and incubated at room temperature for 2 h. The cell membranes were isolated by centrifugation at 25,000*g* for 40 min and then resuspended in solubilization buffer containing 20 mM HEPES, pH 7.5, 100 mM NaCl, 0.5% (w/v) lauryl maltose neopentylglycol (LMNG, Anatrace), 0.1% (w/v) cholesteryl hemisuccinate (CHS, Anatrace), 10% (v/v) glycerol, 10 mM $MgCl_2$, 5 mM $CaCl_2$, 12.5 mU ml^{-1} apyrase, 10 μM TUG-1375, 10 μM PAMs (4-CMTB, compound 187 or AZ-1729), 2.5 μg ml^{-1} leupeptin, 300 μg ml^{-1} benzamidine and 100 μM TECP at 4 °C for 2 h. The supernatant was isolated by centrifugation at 25,000*g* for 40 min, and then incubated with Ni resin at 4 °C overnight. After binding, the resin was washed with a buffer A containing 20 mM HEPES, pH 7.5, 100 mM NaCl, 0.05% (w/v) LMNG, 0.01% (w/v) CHS, 20 mM imidazole, 10 μM TUG-1375, 10 μM PAMs (4-CMTB, compound 187 or AZ-1729), 2.5 μg ml^{-1} leupeptin, 300 μg ml^{-1} benzamidine and 100 μM TECP. The complex was then eluted with buffer A containing 400 mM imidazole. The eluate was supplemented with 2 mM $CaCl_2$ and loaded onto anti-Flag M1 antibody resin. After a washing step, the complex was eluted in buffer A containing 5 mM EDTA and 200 μg ml^{-1} Flag peptide. Finally, a 1.3 molar excess of purified scFv16 was added to the sample. The sample was then loaded onto a Superdex 200 Increase 10/300 column (GE Healthcare) pre-equilibrated with buffer containing 20 mM HEPES pH 7.5, 100 mM NaCl, 0.00075% (w/v) LMNG, 0.00025% (w/v) GDN, 0.00015% (w/v) CHS, 10 μM TUG-1375, 10 μM PAMs (4-CMTB, compound 187 or AZ-1729) and 100 μM TECP. Peak fractions of the complex were collected using an Amicon Ultra Centrifugal Filter (MWCO, 100 kDa).

Cryo-EM sample preparation and data acquisition

For cryo-EM grid preparation of the TUG-1375–4-CMTB–FFA2–$miniG_q$, TUG-1375–compound 187–FFA2–$miniG_q$, TUG-1375–AZ-1729–FFA2–G_i and TUG-1375–compound 187–FFA2–G_i complexes, 3 μl of the purified protein was applied onto glow-discharged holey carbon grids (Quantifoil, Au300 R1.2/1.3). Grids were plunge-frozen in liquid ethane using Vitrobot Mark IV (Thermo Fischer Scientific).

For the TUG-1375–4-CMTB–FFA2–$miniG_q$ and TUG-1375–AZ-1729–FFA2–G_i complexes, cryo-EM imaging was performed on a Titan Krios electron microscope at 300 kV accelerating voltage using a Gatan K3 Summit direct electron detector with an energy filter. A total of 5,535 videos and 9,388 videos were collected with a nominal magnification of ×105,000 using SerialEM[63] software in super-resolution mode at a calibrated pixel size of 0.828 Å and a defocus range of −1.0 to −1.8 μm. Each stack was dose-fractionated to 52 frames with a total dose of 55 e^- Å^{-2}.

For the TUG-1375–compound 187–FFA2–$miniG_q$ and TUG-1375–compound 187–FFA2–G_i complexes, 15,279 videos and 19,526 videos were collected, respectively, using a Titan Krios transmission electron microscope equipped with a Falcon 4i direct electron detector with an energy filter. Images were recorded with a nominal magnification of ×165,000 using EPU3.7 software with a calibrated pixel size of 0.72 Å and a defocus range of −1.0 to −2.0 μm. Each stack was dose-fractionated to 40 frames with a total dose of 55 e^- Å^{-2}.

Data processing, 3D reconstruction and model building

Cryo-EM videos were subjected to patch motion-correction using cryoSPARC[64]. Contrast transfer function (CTF) parameters were calculated using the patch CTF estimation tool.

For the TUG-1375–4-CMTB–FFA2–$miniG_q$ datasets, 5,172,796 particles were autopicked and then subjected to 2D classification to discard bad particles. After ab initio reconstruction and heterogeneous refinement, 309,387 particles were subjected to nonuniform refinement and local refinement, which generated a map with an indicated global resolution of 3.19 Å at a Fourier shell correlation (FSC) of 0.143. To further improve the quality of model of the complex, local refinement focusing on the receptor and the $miniG_q$–scFv16 complex was performed in cryoSPARC, which produced resolutions of 3.26 Å and 3.13 Å, respectively. Local resolution was estimated using cryoSPARC. The maps for the receptor and $miniG_q$–scFv16 complex were combined on the basis of the global map.

For the TUG-1375–compound 187–FFA2–$miniG_q$ datasets, 8,058,394 particles were autopicked and then subjected to 2D classification to discard poorly defined particles. After ab initio reconstruction and heterogeneous refinement, 348,210 particles were subjected to nonuniform refinement and local refinement, which generated a map with an indicated global resolution of 3.06 Å at a FSC of 0.143. Local resolution was estimated using cryoSPARC.

For the TUG-1375–AZ-1729–FFA2–G_i datasets, 8,630,776 particles were autopicked and then subjected to 2D classification to discard poorly defined particles. After ab initio reconstruction and heterogeneous refinement, 161,839 particles were subjected to nonuniform refinement and local refinement, which generated a map with an indicated global resolution of 3.29 Å at a FSC of 0.143. To further improve the quality of the model of the complex, local refinement focusing on the receptor and the G_i–scFv16 complex were performed using cryoSPARC, achieving resolutions of 3.37 Å and 3.23 Å, respectively. Local resolution was estimated using cryoSPARC. The maps for the receptor and G_i–scFv16 complex were combined on the basis of the global map.

For the TUG-1375–compound 187–FFA2–G_i datasets, 11,047,993 particles were initially autopicked and subsequently subjected to 2D classification to exclude low-quality particles. Following ab initio reconstruction and heterogeneous refinement, 271,668 particles

underwent further processing through nonuniform refinement and local refinement. This process produced a map with a global resolution estimated at 3.30 Å based on a FSC of 0.143. To further improve the quality of the model of the complex, local refinement focusing on the receptor and the G_i–scFv16 complex were performed using cryoSPARC, which produced resolutions of 3.38 Å and 3.21 Å, respectively. Local resolution was estimated using cryoSPARC. Finally, maps of the receptor and G_i–scFv16 complex were integrated on the basis of the global map.

The models were built on the basis of previously reported structures. For the TUG-1375–4-CMTB–FFA2–miniG_q–scFv16 and TUG-1375–compound 187–FFA2–miniG_q–scFv16 complexes, the structure of FFA2 and structures of miniG_q and scFv16 obtained from the FFA2–miniG_q–scFv16 complex (PDB accession 8T3S) were used as initial models for docking into the cryo-EM map using Chimera[65,66]. For the TUG-1375–AZ-1729–FFA2–G_i–scFv16 and TUG-1375–compound 187–FFA2–G_i–scFv16 complexes, initial models of FFA2, G_i and scFv16 were obtained from the FFA2–miniG_q–scFv16 complex (PDB accession 8T3S) and the GPR84–G_i–scFv16 complex (PDB accession 8G05). These structures served as initial models for docking into the cryo-EM map using Chimera, which ensured accurate placement in the experimental data. The structures of TUG-1375–4-CMTB–FFA2–miniG_q–scFv16, TUG-1375–compound 187–FFA2–miniG_q–scFv16, TUG-1375–AZ-1729–FFA2–G_i–scFv16 and TUG-1375–compound 187–FFA2-G_i–scFv16 complexes were subsequently generating using iterative manual building and adjustment in Coot[67], followed by real-space refinement in Phenix[68]. The final models were validated using Molprobity[69]. Detailed statistics for data collection, processing and refinement are provided in Extended Data Table 1. Detailed information on the data processing is provided in Extended Data Fig. 2 and Supplementary Figs. 1 and 2. For structural analysis, hydrogen bonds were defined as interactions occurring between two electronegative atoms with a distance less than 3.5 Å.

FFA2 functional assays

Plasmids and mutagenesis. The human FFA2 receptor with either an eYFP or a HA epitope fused to the C terminus was cloned into a pcDNA5/FRT/TO expression vector as previously described[70,71]. Site-directed mutagenesis to generate point mutations was performed according to the QuikChange method (Stratagene). TRUPATH G-protein-dissociation sensors were modified to be expressed through an internal ribosome entry site (IRES)-based plasmid. In brief, TRUPATH-like single plasmid pIRES constructs were generated by cloning G protein β3 (GNB3, Addgene, 140988) upstream of the IRES sequence in pIRES, in-frame with a self-cleavage peptide P2A and with a short GSG linker on either side, and mNeonGreen-γ9 (GFP2 replaced with mNeonGreen from GFP2-γ9, GNGT2, Addgene, 140991). $G\alpha_{i3}$(Addgene, 140975) and $G\alpha_q$ (Addgene, 140982), with *Renilla* luciferase replaced by Nano luciferase, were cloned downstream of the IRES sequence in the above-described construct. In certain experiments, Y356C $G\alpha_q$ replaced $G\alpha_q$.

Cell culture, transfection and generation of cell lines. HEK293T cells (Invitrogen) were maintained in Dulbecco's modified Eagle's medium (DMEM) without sodium pyruvate, supplemented with 10% (v/v) FBS and 1% penicillin–streptomycin, at 37 °C in a 5% CO_2 humidified atmosphere.

Flp-In TREx 293 cells (Invitrogen) were maintained in DMEM without sodium pyruvate, supplemented with 10% (v/v) FBS, 1% penicillin–streptomycin and 10 μg ml^{-1} blasticidin, at 37 °C in a 5% CO_2 humidified atmosphere.

To generate Flp-In TREx 293 cells expressing the various FFA2–eYFP receptor constructs in an inducible manner, cells were transfected with a mixture containing the desired cDNA in a pcDNA5/FRT/TO vector and a pOG44 vector (1:9) by using 1 mg ml^{-1} PEI (MW-25000). Cells were plated until 60–80% confluent then transfected with 8 μg of the required plasmid DNA and PEI (ratio of 1:6 DNA to PEI), diluted in 150 mM NaCl, pH 7.4. After incubation at room temperature for 10 min, the mixture was added to cells. After 48 h, the medium was changed to medium supplemented with 200 μg ml^{-1} hygromycin B to initiate the selection of stably transfected cells. After isolation of resistant cells, expression of the appropriate construct from the Flp-In TREx locus was induced by adding up to 100 ng ml^{-1} doxycycline for 24 h.

BRET β-arrestin 1 and β-arrestin 2 recruitment assays. HEK293T cells were co-transfected at a 100:1 ratio with plasmids encoding an eYFP-tagged form of the receptor construct of interest and either β-arrestin 1 or β-arrestin 2 tagged with Nano-luciferase. Cells were transferred into white 96-well microtitre plates at 24 h after transfection. The following day, cells were washed, and the culture medium replaced with Hanks' balanced salt solution (HBSS) immediately before conducting the assay. To measure β-arrestin 1 or β-arrestin 2 recruitment to the receptor, the Nano-luciferase substrate coelenterazine H was added to a final concentration of 5 μM, and cells were incubated for a further 10 min at 37 °C. After addition of ligand at 37 °C for 5 min, BRET resulting from receptor–arrestin proximity was assessed by measuring the ratio of luminescence at 535 and 475 nm using a PHERAstar FS plate reader fitted with the BRET1 optic module (BMG Labtech).

TRUPATH assays. HEK293T cells were transiently transfected using PEI and a total of 5 μg per 10 cm dish plasmid DNA with receptor, biosensor and pcDNA3.1 at a ratio of 1:2.5:1.5. Cells were transferred into white 96-well microtitre plates 24 h after transfection. The following day, cells were washed, and the culture medium was replaced with HBSS immediately before conducting the assay. To measure G protein dissociation, the Nano-luciferase substrate NanoGlo was added at a 1:80 final dilution in HBSS, and cells were incubated for 10 min at 37 °C. After a further 5 min of incubation with ligand, BRET was assessed as described above.

HTRF-based cAMP-inhibition assays. All cAMP experiments were performed using Flp-In T-REx 293 cells induced to express the receptor construct of interest. Experiments were carried out using a homogenous time-resolved fluorescence resonance energy transfer (FRET) (HTRF)-based detection kit (Revvity) according to the manufacturer's protocol. For the assay, cells were plated at 2,500 cells per well in low-volume 384-well plates. The ability of ligands to inhibit 1 μM forskolin-induced cAMP production was assessed after 1 h of incubation with ligand. Reactions were stopped according to the manufacturer's instructions, and the output was measured using a PHERAstar FS plate reader (BMGLabtech).

[^{35}S]GTPγS-binding assays. Membranes were generated from Flp-In T-REx 293 cells after 100 ng ml^{-1} doxycycline treatment to induce receptor expression. Cells were washed with ice-cold PBS, removed from dishes by scraping and centrifuged at 1,800*g* for 5 min at 4 °C. Pellets were resuspended in TE buffer (10 mM Tris-HCl and 0.1 mM EDTA, pH 7.5) containing a protease inhibitor mixture (Roche) and homogenized with a 5 ml hand-held homogenizer. Samples were centrifuged at 450*g* for 5 min at 4 °C and the supernatant was further centrifuged at 90,000*g* for 45 min at 4 °C. The resulting pellet was resuspended in TE buffer and protein content was assessed using a BCA protein assay kit (Thermo Fisher Scientific).

Prepared membrane protein (5 μg per well) was incubated in assay buffer (20 mM HEPES, 5 mM $MgCl_2$, 160 mM NaCl and 0.1% fatty-acid-free BSA, pH 7.5) containing the indicated ligand concentrations. The reaction was initiated by the addition of [^{35}S]GTPγS (100 nCi per reaction) with 1 μM GDP and incubated at 30 °C for 60 min. The reaction was terminated by rapid vacuum filtration through GF/C glassfibre filter-bottom 96-well microplates (Revvity) using a UniFilter FilterMate Harvester (PerkinElmer). Unbound radioligand was removed from filters by three washes with ice-cold PBS. MicroScint-20 (Revvity) was

added to dried filters and [^{35}S]GTPγS binding was quantified by liquid scintillation spectroscopy.

Radioligand-binding assays. Assays were performed on membranes generated from Flp-In T-REx 293 cells with increasing concentrations of [^{3}H] GLPG0974, binding buffer (50 mM Tris-HCl, 100 mM NaCl, 10 mM $MgCl_2$ and 1 mM EDTA, pH 7.4), in a total assay volume of 500 µl in 96-deep-well blocks. Binding was initiated by the addition of membranes (5 µg of protein per well). All assays were performed at 25 °C for 2 h before termination by the addition of ice-cold PBS and vacuum filtration through GF/C glassfibre filter-bottom 96-well microplates. Plates were washed 3 times with ice-cold PBS then allowed to dry for 2–3 h at room temperature. MicroScint-20 was added to the dried filter plates, and radioactivity was quantified by liquid scintillation spectrometry. Specific binding was defined as the difference between binding detected in the presence and absence of 10 µM CATPB.

For saturation-binding curves, the specific binding versus radioligand concentration was fit to a one-site specific binding model, where B_{max} and K_d values for the radioligand were calculated. For all other concentration–response curves, data were fit to a three-parameter sigmoidal concentration–response curve. In all FFA2 functional assays, HEK293T and Flp-In T-REx 293 cells were authenticated by Northgene (case numbers C-24809a and C-24809b). They were confirmed to be mycoplasma-free and were tested for mycoplasma every 3 months.

Molecular docking and dynamic simulations

Molecular docking was performed using Schrodinger GLIDE[72], and loop refinement and other structure modifications were conducted using Schrodinger Maestro 2021-3 suite[73]. Probe-confined dynamic mapping was performed following a modified version of our published protocol[42] using AmberTools 23 (ref. 74), VMD (v.1.9.3)[75] and HTMD (v.2.3.2/2.3.36)[76], and receptor conformations taken from these simulations were used to predict the binding modes of AZ-1729 (root mean square deviation (r.m.s.d) from the cryo-EM structure of 1.87 Å) and compound 187 (r.m.s.d. from the cryo-EM structure of 1.61 Å). MD simulations were performed under ago-PAM removal and in PAM-only conditions using a variety of FFA2 cryo-EM structures and docked structures (Extended Data Fig. 5 and Supplementary Table 1). Membrane-bilayer systems with FFA2 placed in a 1-palmitoyl-2-oleoyl-*sn*-glycero-3-phosphocholine (POPC) membrane were prepared using the CHARMM-GUI web-server[77] and simulated in AMBER20 (ref. 78) at 37 °C temperature with tip3p water model[79] and ff19SB[80], lipid21 (ref. 81) and GAFF2 (ref. 82) force fields for protein, lipid and ligand molecules, respectively. Simulations were analysed using AmberTools 23 (ref. 74) along with MDAnalysis (v.2.7.0)[83,84] and SciKit Learn (v.1.5.1)[85] Python libraries. Detailed methods regarding docking and MD simulations are included in the Supplementary Information. Detailed r.m.s.d. and root mean square fluctuation data for all simulated systems and residue–ligand interaction energy values are provided in Supplementary Tables 1 and 2.

Reporting summary

Further information on research design is available in the Nature Portfolio Reporting Summary linked to this article.

Data availability

The 3D cryo-EM density maps of the structures of FFA2 signalling complexes have been deposited into the Electron Microscopy Data Bank under the accession numbers EMD-45732 for TUG-1375–4-CMTB–FFA2–miniG_q, EMD-45738 for TUG-1375–compound 187–FFA2–miniG_q, EMD-45743 for TUG-1375–AZ-1729–FFA2–G_i and EMD-49745 for TUG-1375–compound 187–FFA2–G_i. Atomic coordinates for the atomic models have been deposited into the PDB under the accession numbers 9CLW for TUG-1375–4-CMTB–FFA2–miniG_q, 9CM3 for TUG-1375–compound 187–FFA2–miniG_q, 9CM7 for TUG-1375–AZ-1729–FFA2–G_i and 9NS9 for TUG-1375–compound 187–FFA2–G_i. The following structural data used for comparisons are available from the PDB: 7LD3 (the A_1R bound to the PAM MIPS521)[38]; 8J22 (TUG-1375-bound FFA2 coupled with G_i)[22]; 8J23 (empty FFA2 coupled with G_i); 8T3S (C4-bound FFA2 coupled with miniG_q)[21]; 8J21 (C4-bound FFA3 coupled with G_i)[22]; 8G05 (GPR84 coupled with G_i)[86]; and 6C1R (C5aR bound to PMX53 and avacopan)[60]. Simulation trajectories were uploaded to GPCRmd (https://www.gpcrmd.org/)[87] and linked to the current paper. Simulation identifiers are provided in Supplementary Table 3.

62. Liu, P. et al. The structural basis of the dominant negative phenotype of the $G\alpha_i\beta_1\gamma_2$ G203A/A326S heterotrimer. *Acta Pharmacol. Sin.* **37**, 1259–1272 (2016).
63. Mastronarde, D. N. Automated electron microscope tomography using robust prediction of specimen movements. *J. Struct. Biol.* **152**, 36–51 (2005).
64. Punjani, A., Rubinstein, J. L., Fleet, D. J. & Brubaker, M. A. cryoSPARC: algorithms for rapid unsupervised cryo-EM structure determination. *Nat. Methods* **14**, 290–296 (2017).
65. Pettersen, E. F. et al. UCSF Chimera—a visualization system for exploratory research and analysis. *J. Comput. Chem.* **25**, 1605–1612 (2004).
66. Pettersen, E. F. et al. UCSF ChimeraX: structure visualization for researchers, educators, and developers. *Protein Sci.* **30**, 70–82 (2021).
67. Emsley, P. & Cowtan, K. Coot: model-building tools for molecular graphics. *Acta Crystallogr. D Biol. Crystallogr.* **60**, 2126–2132 (2004).
68. Adams, P. D. et al. PHENIX: a comprehensive Python-based system for macromolecular structure solution. *Acta Crystallogr. D Biol. Crystallogr.* **66**, 213–221 (2010).
69. Chen, V. B. et al. MolProbity: all-atom structure validation for macromolecular crystallography. *Acta Crystallogr. D Biol. Crystallogr.* **66**, 12–21 (2010).
70. Stoddart, L. A., Smith, N. J., Jenkins, L., Brown, A. J. & Milligan, G. Conserved polar residues in transmembrane domains V, VI, and VII of free fatty acid receptor 2 and free fatty acid receptor 3 are required for the binding and function of short chain fatty acids. *J. Biol. Chem.* **283**, 32913–32924 (2008).
71. Bolognini, D. et al. Chemogenetics defines receptor-mediated functions of short chain free fatty acids. *Nat. Chem. Biol.* **15**, 489–498 (2019).
72. Glide Release 2021-3 (Schrödinger, 2021).
73. Maestro Release 2021-3 (Schrödinger, 2021).
74. AMBER 2023 (Univ. California, San Francisco, 2023).
75. Humphrey, W., Dalke, A. & Schulten, K. VMD: visual molecular dynamics. *J. Mol. Graph.* **14**, 33–38 (1996).
76. Doerr, S., Harvey, M. J., Noe, F. & De Fabritiis, G. HTMD: high-throughput molecular dynamics for molecular discovery. *J. Chem. Theory Comput.* **12**, 1845–1852 (2016).
77. Lee, J. et al. CHARMM-GUI supports the Amber force fields. *J. Chem. Phys.* **153**, 035103 (2020).
78. AMBER 2020 (Univ. California, San Francisco, 2020).
79. Jorgensen, W. L., Chandrasekhar, J., Madura, J. D., Impey, R. W. & Klein, M. L. Comparison of simple potential functions for simulating liquid water. *J. Chem. Phys.* **79**, 926–935 (1983).
80. Tian, C. et al. ff19SB: amino-acid-specific protein backbone parameters trained against quantum mechanics energy surfaces in solution. *J. Chem. Theory Comput.* **16**, 528–552 (2020).
81. Dickson, C. J., Walker, R. C. & Gould, I. R. Lipid21: complex lipid membrane simulations with AMBER. *J. Chem. Theory Comput.* **18**, 1726–1736 (2022).
82. He, X., Man, V. H., Yang, W., Lee, T. S. & Wang, J. A fast and high-quality charge model for the next generation general AMBER force field. *J. Chem. Phys.* **153**, 114502 (2020).
83. Gowers, R. J et al. MDAnalysis: A Python package for the rapid analysis of molecular dynamics simulations. In *Proc. 15th Python in Science Conference* (eds Benthall, S. & Rostrup, S.) 98–105 (SciPy, 2016).
84. Michaud-Agrawal, N., Denning, E. J., Woolf, T. B. & Beckstein, O. MDAnalysis: a toolkit for the analysis of molecular dynamics simulations. *J. Comput. Chem.* **32**, 2319–2327 (2011).
85. Pedregosa, F. et al. Scikit-learn: machine learning in Python. *J. Mach. Learn. Res.* **12**, 2825–2830 (2011).
86. Zhang, X. et al. Pro-phagocytic function and structural basis of GPR84 signaling. *Nat. Commun.* **14**, 5706 (2023).
87. Rodriguez-Espigares, I. et al. GPCRmd uncovers the dynamics of the 3D-GPCRome. *Nat. Methods* **17**, 777–787 (2020).

Acknowledgements We thank the cryo-EM facility directed by J. Conway and partially supported by the grants S10 OD025009 (Krios) and S10 OD019995 (Falcon 2/3 camera) from the National Institutes of Health (NIH). This work was supported by NIH grant R35GM128641 (to C.Z.), Medical Research Council grant MR/X010198/1 (to G.M.), Biotechnology and Biological Sciences Research Council grants BB/R001480/1 and BB/S000453/1 (to G.M.) and BB/R007101/1 (to I.G.T.), Lundbeck Foundation grant R307-2018-2950 (to E.R.U.), and the Novo Nordisk Foundation grant NNF21OC0069019 (to T.U.). A.-A.G.'s PhD study is supported by the MSCA COFUND CITI-GENS Programme funded by the EU Horizon 2020 research and innovation programme (grant agreement no. 945231). This project made use of computational time on Kelvin-2 supported by the Engineering and Physical Sciences Research Council (EPSRC) (grant numbers EP/T022175/1 and EP/W03204X/1) and ARCHER2 granted through the UK High-End Computing Consortium for Biomolecular Simulation, HECBioSim (https://www.hecbiosim.ac.uk), supported by the EPSRC (grant numbers EP/R029407/1 and EP/W03204X/1).

Author contributions C.Z., G.M. and I.G.T. conceived the project and designed the research with X.Z. X.Z. performed protein expression and purification studies, screened the cryo-EM grids, collected the cryo-EM data and processed the data under the supervision of C.Z. L.J. and S.M. performed pharmacological and mutagenesis studies under the supervision of G.M.

A.-A.G. performed the computational analyses under the supervision of I.G.T. G.M. and I.G.T. analysed data. A.V. and K.S.-K. performed compound synthesis and pharmacological characterizations under the supervision of T.U. and E.R.U. C.Z. wrote the manuscript together with G.M. and I.G.T. with help from X.Z., A.-A.G., L.J., E.R.U. and T.U.

Competing interests G.M. and T.U. are co-founders and directors of Caldan Therapeutics (https://www.caldantherapeutics.com/). G.M. is a co-founder and director of KelticPharmaTherapeutics (https://keltic-pharma.com/). Both companies have interests in the development of FFA4 activators. The other authors declare no competing interests.

Additional information

Supplementary information The online version contains supplementary material available at https://doi.org/10.1038/s41586-025-09186-6.

Correspondence and requests for materials should be addressed to Irina G. Tikhonova, Graeme Milligan or Cheng Zhang.

Peer review information *Nature* thanks Asuka Inoue, Maria Marti-Solano and the other, anonymous, reviewer(s) for their contribution to the peer review of this work. Peer reviewer reports are available.

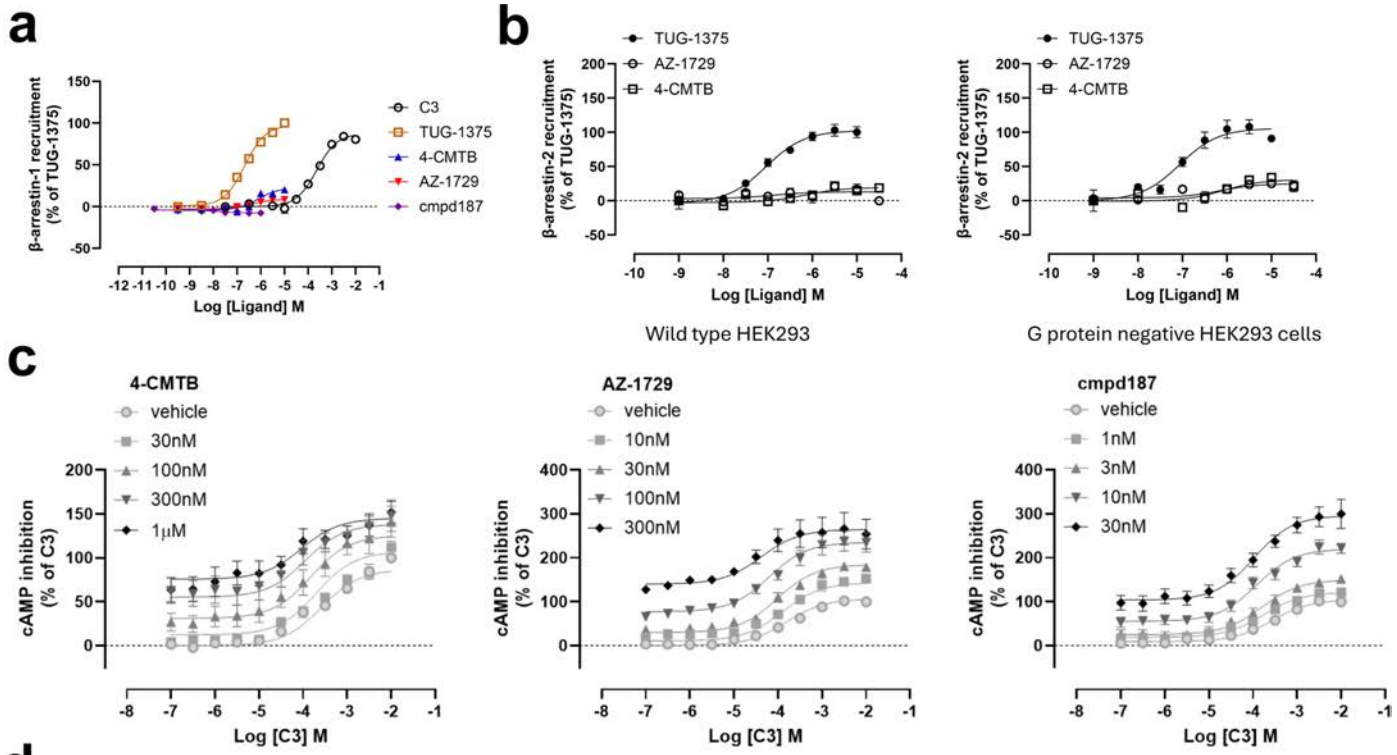

d

Agonist [a]	Modulator [b]	pK_A [c]	pK_B [d]	logα	logβ	gain in potency [e]	gain in efficacy [f]
TUG-1375	4-CMTB	6.25 ± 0.15	5.53 ± 0.08	1.08 ± 0.28	0.57 ± 0.15	+ 0.92 **	ns
TUG-1375	AZ-1729	6.29 ± 0.09	6.08 ± 0.25	0.40 ± 0.48	1.50 ± 0.32	+ 0.81 **	+ 168 **
TUG-1375	cmpd187	nd	nd	nd	nd	ns	+ 297 ****
AZ-1729	TUG-1375	5.93 ± 0.13	6.41 ± 0.18	0.67 ± 0.16	0.58 ± 0.08	+ 0.99 **	ns
AZ-1729	4-CMTB	5.95 ± 0.23	6.22 ± 0.12	0.69 ± 0.19	0.34 ± 0.09	+ 1.39 *	ns
AZ-1729	cmpd187	nd	nd	nd	nd	ns	ns
cmpd187	4-CMTB	nd	nd	nd	nd	+ 0.38 **	+ 279 **

Agonist [a]	Modulator [b]	pK_A [c]	pK_B [d]	logα	logβ	gain in potency [e]	gain in efficacy [f]
C3	4-CMTB	3.31 ± 0.13	6.42 ± 0.12	0.34 ± 0.26	0.69 ± 0.13	+ 0.76 **	ns
C3	AZ-1729	3.64 ± 0.12	6.05 ± 0.26	0.45 ± 0.37	1.34 ± 0.18	+ 0.98 **	+ 154 *
C3	187	nd	nd	nd	nd	ns	+ 214 ***

Extended Data Fig. 1 | See next page for caption.

Extended Data Fig. 1 | Pharmacological characterization of FFA2 ligands. **a**. β-arrestin 1 recruitment induced by FFA2 activators and modulators. **b**. β-arrestin 2 recruitment induced by FFA2 activators and modulators in wild-type HEK293T and G protein deficient (ΔG_s, ΔG_{12}, ΔG_{13}, ΔG_q, ΔG_{11} + Pertussis toxin treatment to inactivate Gi-family G proteins) HEK293T cells. Data are means +/− S.E.M. n = 3 (three biologically independent experiments). **c**. Cooperativity of function between three FFA2 PAMs and the orthosteric agonist C3 (propionate). The ability of the indicated concentrations of 4-CMTB, compound 187, and AZ-1729 to modulate inhibition of forskolin-stimulated levels of cAMP via FFA2 is shown. Data are means +/− S.E.M. n = 3 (three biologically independent experiments). **d**. Binding characteristics of FFA2 modulators assessed in co-operativity studies. [a]Agonist refers to the compound used to generate concentration-response curve. [b]Modulator is the compound used in defined concentrations. [c]pK_A represents values estimated for the agonist. [d]pK_B represents values estimated for the modulator. [e]Gain in potency was calculated using the equation (pEC_{50} agonist + highest concentration of modulator) - (pEC_{50} agonist + vehicle). [f]Gain in efficacy was calculated using the equation (Emax agonist + highest concentration of modulator) - (Emax agonist + vehicle). nd means not determined (in experiments in which the effect of compound 187 was largely manifest in terms of efficacy and thus affinity values could not be derived). Emax was constrained to the maximal possible system response and n was constrained to 1 (the slope factor). Statistical significance was determined using one-way ANOVA followed by Dunnett's multiple comparisons test; *p < 0.05, **p < 0.01, ****p < 0.0001, ns denotes not significant. Cmpd187 refers to compound 187.

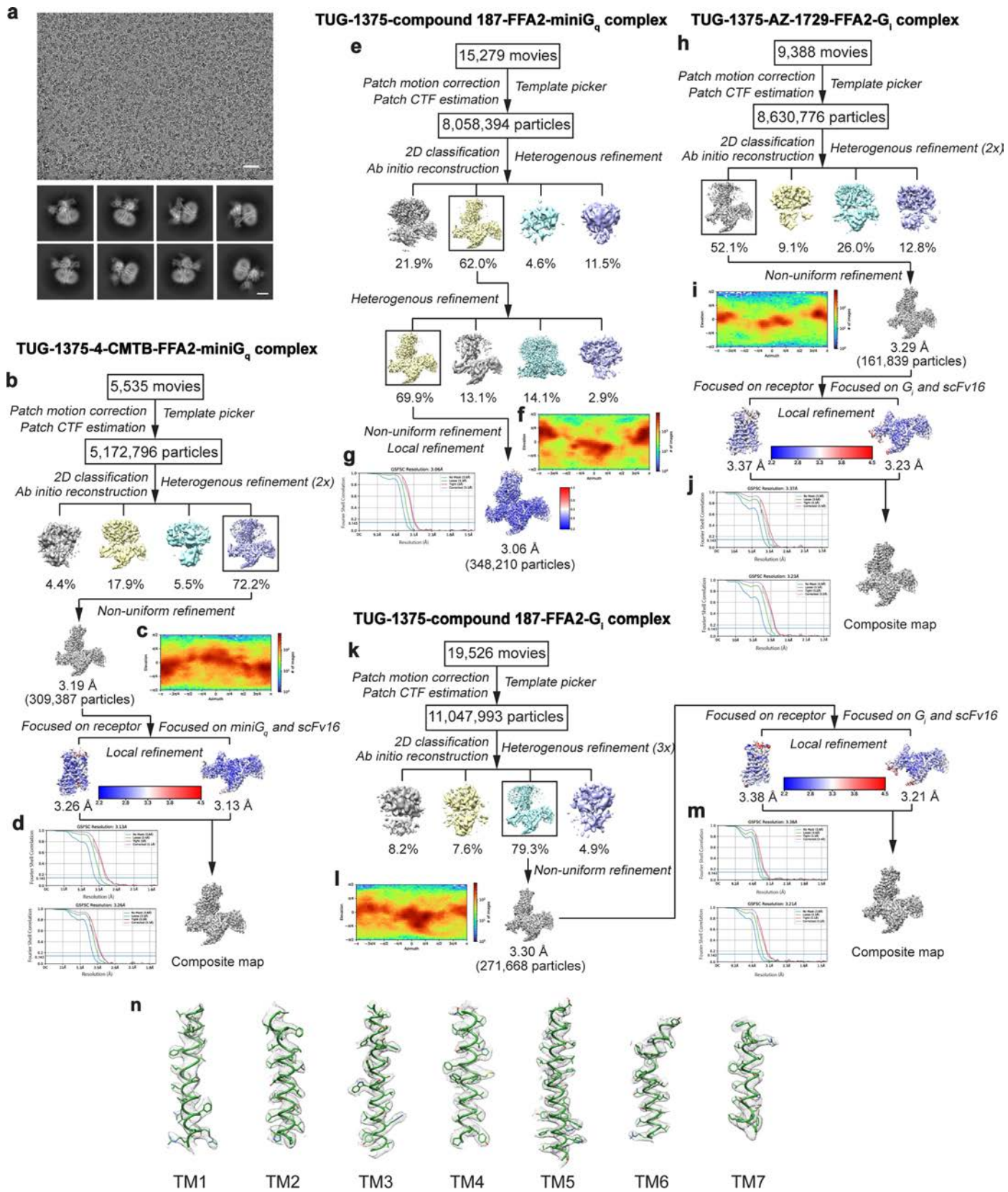

Extended Data Fig. 2 | See next page for caption.

Extended Data Fig. 2 | Cryo-EM data processing and analysis. **a**, Representative cryo-EM micrograph (scale bar: 50 nm) and 2D class averages (scale bar: 5 nm). The micrograph shown is one example of 5535 micrographs for miniG_q-coupled FFA2 bound to TUG-1375 and 4-CMTB. **b**-**m**, Cryo-EM image processing workflow for TUG-1375-4-CMTB-FFA2-miniG_q complex (**b**-**d**), TUG-1375-compound 187-FFA2-miniG_q complex (**e**-**g**), TUG-1375-AZ-1729-FFA2-G_i complex (**h**-**j**), and TUG-1375-compound 187-FFA2-G_i complex (**k**-**m**), respectively. Detailed information on protein purification is provided in Supplementary Fig. 1. Angular distributions of the particles used in the final reconstruction are shown in **c** for TUG-1375-4-CMTB-FFA2-miniG_q complex; **f** for TUG-1375-compound 187-FFA2-miniG_q complex; **i** for TUG-1375-AZ-1729-FFA2-G_i complex; and **l** for TUG-1375-compound 187-FFA2-G_i complex. Gold-standard Fourier shell correlation (FSC) curves are shown in **d** for TUG-1375-4-CMTB-FFA2-miniG_q complex; **g** for TUG-1375-compound 187-FFA2-miniG_q complex; **j** for TUG-1375-AZ-1729-FFA2-G_i complex; and **m** for TUG-1375-compound 187-FFA2-G_i complex. **n**, Cryo-EM maps and models of the seven transmembrane helices (TM1-7) of miniG_q-coupled FFA2 bound to TUG-1375 and 4-CMTB. Representative cryo-EM maps of FFA2 in other complexes and ligands are shown in Supplementary Fig. 2.

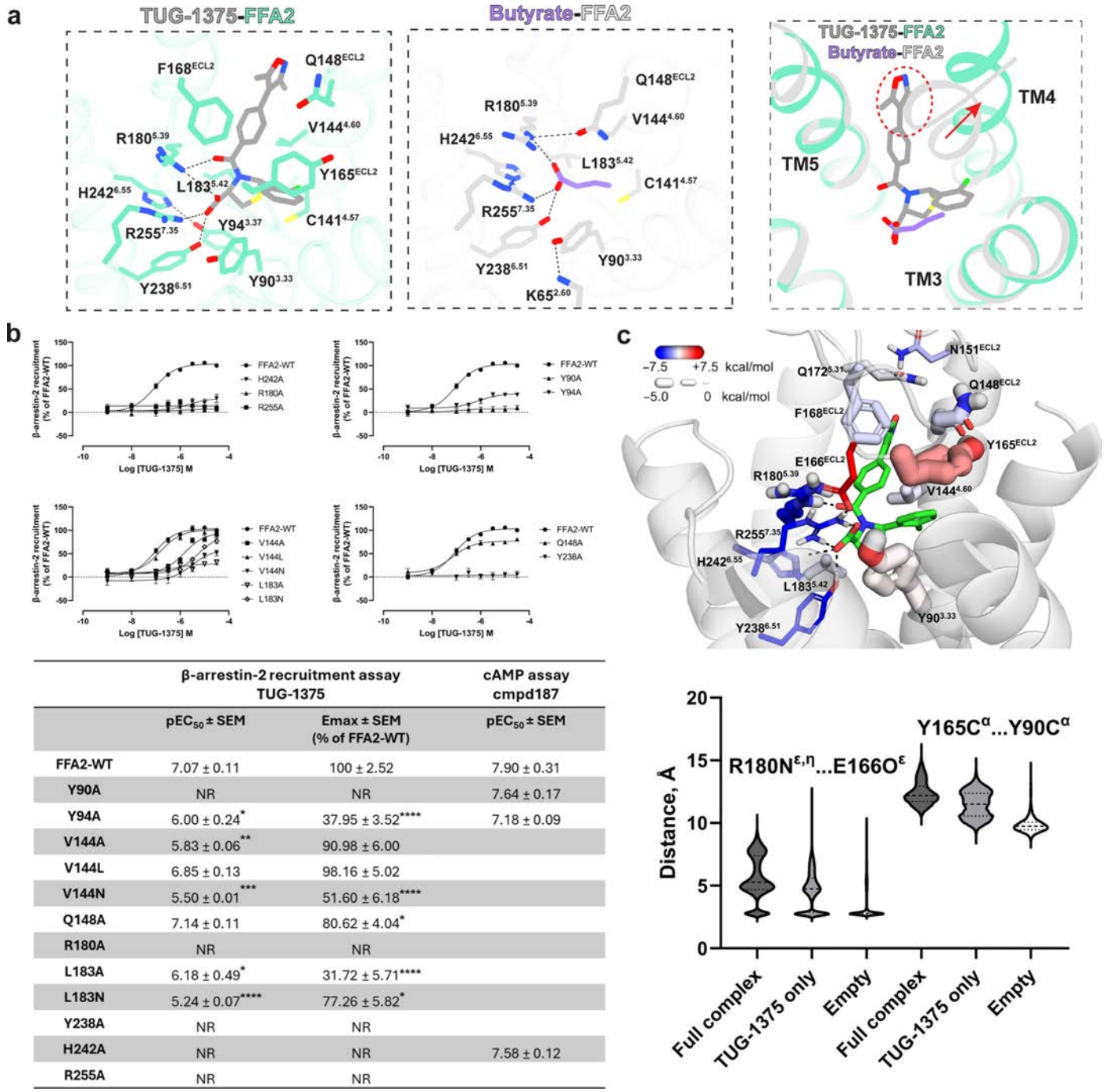

	β-arrestin-2 recruitment assay TUG-1375		cAMP assay cmpd187
	pEC_{50} ± SEM	Emax ± SEM (% of FFA2-WT)	pEC_{50} ± SEM
FFA2-WT	7.07 ± 0.11	100 ± 2.52	7.90 ± 0.31
Y90A	NR	NR	7.64 ± 0.17
Y94A	6.00 ± 0.24*	37.95 ± 3.52****	7.18 ± 0.09
V144A	5.83 ± 0.06**	90.98 ± 6.00	
V144L	6.85 ± 0.13	98.16 ± 5.02	
V144N	5.50 ± 0.01***	51.60 ± 6.18****	
Q148A	7.14 ± 0.11	80.62 ± 4.04*	
R180A	NR	NR	
L183A	6.18 ± 0.49*	31.72 ± 5.71****	
L183N	5.24 ± 0.07****	77.26 ± 5.82*	
Y238A	NR	NR	
H242A	NR	NR	7.58 ± 0.12
R255A	NR	NR	

Extended Data Fig. 3 | See next page for caption.

Extended Data Fig. 3 | TUG-1375 binding in the orthosteric binding pocket. **a**, Left and middle panels show the comparison of the receptor interaction profiles of TUG-1375 and butyrate (C4) with FFA2. The binding profile of TUG-1375 is based on the structure of miniG_q-coupled FFA2 in complex with TUG-1375 and compound 187, while the C4 binding profile is derived from our previously published structure (PDB ID: 8T3S). Polar interactions are shown as black dashed lines. Right panel shows the outward movement of TM4 in the structure of FFA2 with TUG-1375 compared to that with C4 (butyrate) indicated by the red arrow. The red circle indicates the group of TUG-1375 that causes such movement. **B**, Effects of mutations within the orthosteric pocket on the function of TUG-1375 measured by β-arrestin 2 recruitment. Detailed calculations based on the concentration-response curves (upper) are summarized in the table (lower). pEC_{50} of TUG-1375 and efficacy compared to that of TUG-1375 at wild type (WT) human FFA2 was assessed for the indicated point mutants of the receptor by β-arrestin 2 recruitment assays. For the indicated mutants, the ability of compound 187 to inhibit forskolin stimulated levels of cAMP in cells stably expressing eYFP-tagged forms of the receptor was used to confirm expression and function of an appropriately processed and cell surface delivered form of FFA2. Data are means +/− s.e.m. n = 3 (three biologically independent experiments). Statistical significance was assessed by one way ANOVA followed by Dunnett's multiple comparison test. * $p < 0.05$, ** $p < 0.01$, *** $p < 0.001$, **** $p < 0.0001$. NR means no detectable response. **c**, MD simulations on TUG-1375 binding. The upper panel shows a representative simulation frame depicting TUG-1375 in the orthosteric binding pocket, with key interacting residues shown as sticks. Residue carbon colors and stick thickness represent average electrostatic and van der Waals interaction energies between each residue and the ligand, respectively. Dashed lines indicate hydrogen bonds. The lower panel shows violin plots indicating the distribution of distances between the guanidyl fragment of $R180^{5.39}$ and the carboxylic group of $E166^{ECL2}$ (left) and between the Cα atoms of $Y165^{ECL2}$ and $Y90^{3.33}$ (right) across three 1 μs replicates of FFA2/4-CMTB/TUG-1375/miniG_q (Full complex), FFA2/TUG-1375 (TUG-1375 only, without the G protein), and empty FFA2 (Empty, without the ligand and G protein). The results revealed that TUG-1375 affects the ECL2 conformation and the top of TM4. Upon ligand removal, the orthosteric pocket shrinks significantly due to a major conformational change in ECL2, with $E166^{ECL2}$ and $Y165^{ECL2}$ shifting towards $R180^{5.39}$ and $Y90^{3.33}$, respectively, forming extensive electrostatic and aromatic contacts. Detailed analysis of TUG-1375 binding can be found in Supplementary Information. Cmpd187 refers to compound 187.

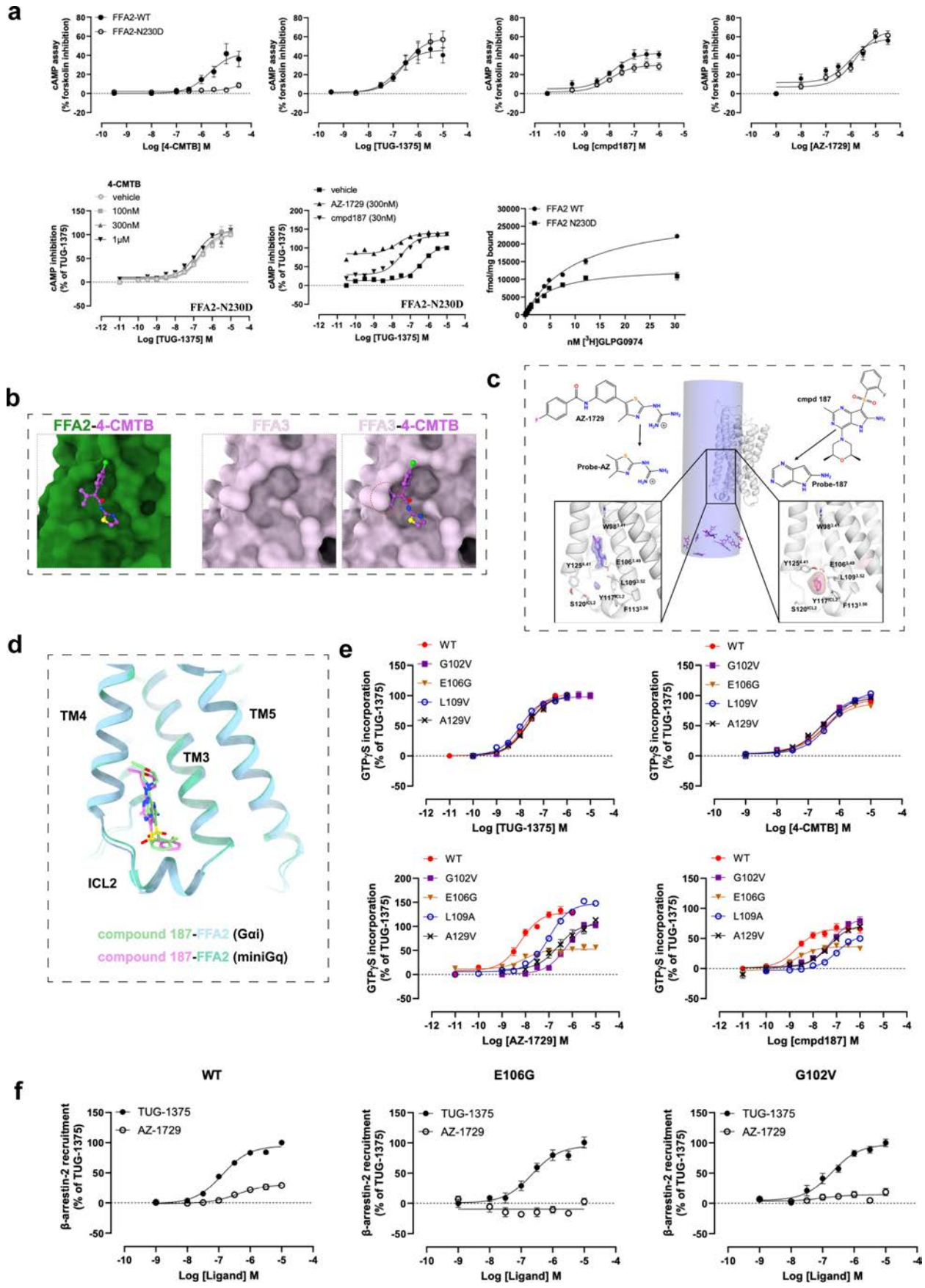

Extended Data Fig. 4 | See next page for caption.

Extended Data Fig. 4 | Binding properties of FFA2 ago-PAMs at Site 1 and 2. **a**, Loss of agonist activity and cooperativity with TUG-1375 for 4-CMTB at $N^{230}D$ FFA2, as measured by cAMP reduction assays. The data in the top row show that 4-CMTB lacks agonist action at $N^{230}D$ FFA2 whilst TUG-1375, compound 187 and AZ-1729 all activate this mutant as effectively as wild type. The data in the left and the middle panel of the bottom row indicate that 4-CMTB does not produce co-operativity with TUG-1375 at $N^{230}D$ FFA2 (left), while such effects of both AZ-1729 and compound 187 are retained at this mutant (middle). The data in the right panel indicate that the human FFA2 antagonist [^{3}H]GLPG0974 displays high affinity binding to both wild type and $N^{230}D$ FFA2. Data are means +/− S.E.M. n = 3 (three biologically independent experiments). **b**, Structural comparison of FFA2 and FFA3 at Site 1. FFA2 and FFA3 are shown in green and pink, respectively. The space in FFA3 (middle panel, based on the structure PDB ID 8J21) corresponding to Site 1 in FFA2 (left panel) adopts a distinct conformation, which would result in a steric clash with 4-CMTB if it were to adopt a similar binding pose (right panel). **c**, Co-solvent simulations of AZ-1729 and compound 187. The middle figure shows the orthosteric ligand C4 and the probes as they are placed before the simulation, along with the cylinder (semi-transparent, blue) confining the probes around the area of interest, around ICL2. The top left figure shows AZ-1729 and the probe that allowed to identify its interaction with $E106^{3.49}$. The top right figure shows compound 187 and its probe molecule. The bottom left and right figures show the snapshots of the probe-AZ and probe-187, respectively, in MD simulations with the semi-transparent surface denoting the volume occupied by the probe for > 20% of the simulation time. **d**, Structural alignment of Site 2 for compound 187 in the structures with miniG_q and G_i. The interaction profile of compound 187 and the overall conformation of Site 2 including ICL2 are almost identical in these two structures. **e**, Effects of mutations in Site 2 on the potency of FFA2 modulators measured by [^{35}S]GTPγS binding assays. Data are means +/− s.e.m. for at least 3 experiments. pEC_{50} and E_{max} values are listed in Extended Data Table 2. **f**, Undetectable β-arrestin-2 recruitment by AZ-1729 at Site 2 mutations in FFA2. β-arrestin-2 recruitment assays were performed with varying concentrations of TUG-1375 or AZ-1729 at wild type, E106G, and G102V FFA2. Data are means +/− s.e.m. n = 3 (three biologically independent experiments). Cmpd187 refers to compound 187.

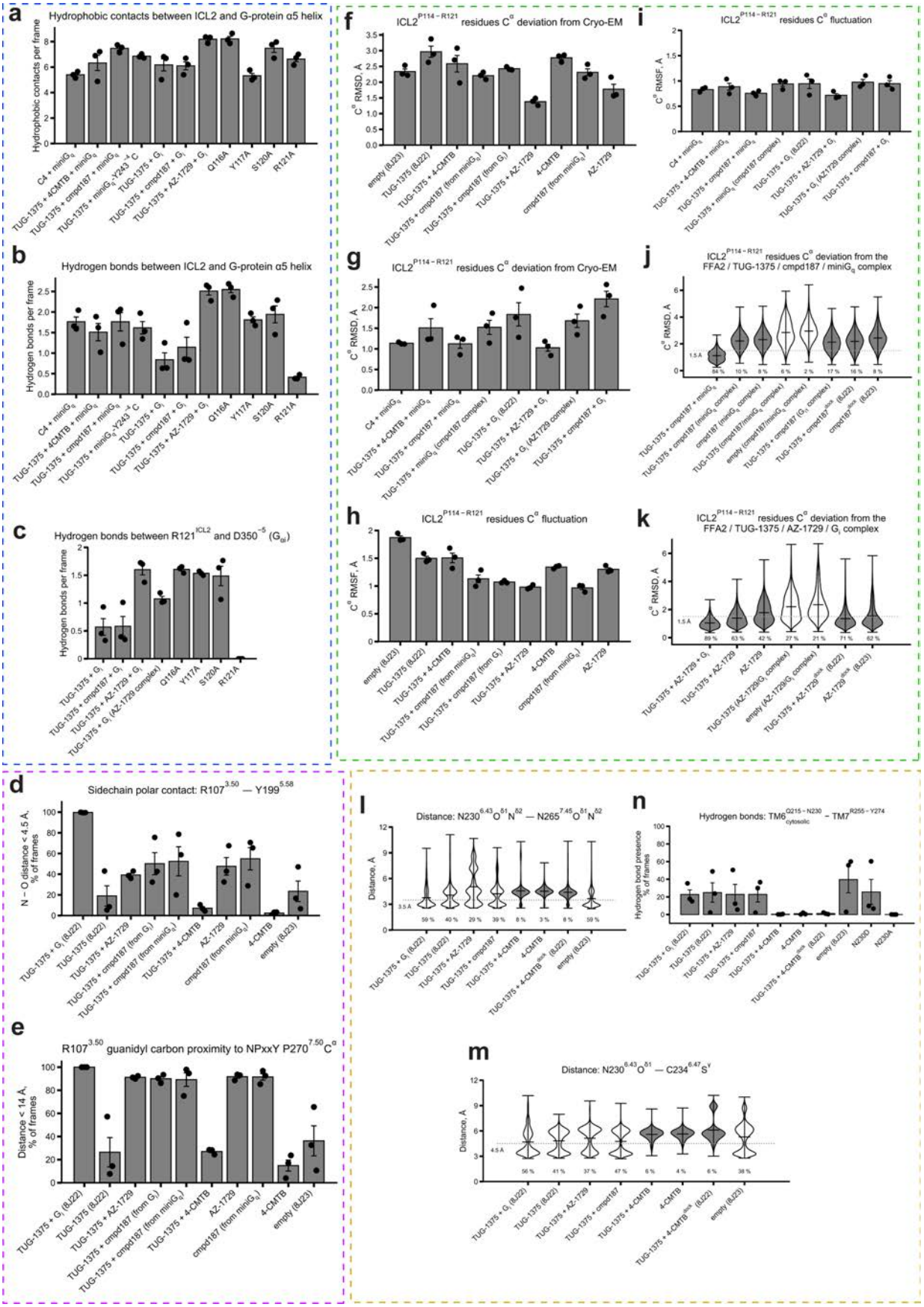

Extended Data Fig. 5 | See next page for caption.

Extended Data Fig. 5 | Molecular dynamics analysis of FFA2 conformational changes and interactions upon different ligand binding and G protein coupling. a-c, Molecular interactions between FFA2 ICL2 and G protein. **a**, Hydrophobic contacts between ICL2 (P114-R121) and G protein α5 helix. Data show mean number of carbon-carbon contacts (≤ 4 Å) per frame ± s.e.m. from three independent 1 µs simulations (n = 3). Individual replicate values shown as black dots. AZ-1729/G_i complex shows enhanced contacts compared to TUG-1375 alone, with significant reduction in Y117A mutant. **b**, Hydrogen between ICL2 and G protein α5 helix. Data show mean number of hydrogen bonds (D-A distance ≤3.5 Å, angle 180 ± 30°) per frame ± s.e.m. from three independent 1 µs simulations (n = 3). Individual replicate values shown as black dots. AZ-1729 enhances hydrogen bonding with G_i, while R121A mutation shows the strongest reduction in these interactions. **c**, Hydrogen bonds between $R121^{ICL2}$ and $D350^{H5.22}$ of G_i. Data show mean number of hydrogen bonds per frame ± s.e.m. from three independent 1 µs simulations (n = 3). Individual replicate values shown as black dots. Enhanced interactions in AZ-1729 complex and complete loss with R121A mutation. **d-e**, Analysis of $R^{3.50}$ interactions with $Y^{5.58}$ and the distance between $R^{3.50}$ and D/$NP^{7.50}$xxY motif in FFA2. **d**, Sidechain polar contacts between $R107^{3.50}$ and $Y199^{5.58}$. Data show percentage of frames with nitrogen-to-oxygen distance <4.5 Å ± s.e.m. from three independent 1 µs simulations (n = 3). Individual replicate values shown as black dots. **e**, Proximity between $R107^{3.50}$ guanidyl carbon and $P270^{7.50}$ Cα. Data show percentage of frames with distance <14 Å ± s.e.m. from three independent 1 µs simulations (n = 3). Individual replicate values shown as black dots. **f-k**, Conformational stability analysis of ICL2. **f-g**, Root-mean-square deviation (RMSD) of ICL2 residues P114-R121. Data show mean RMSD ± s.e.m. from three independent 1 µs simulations (n = 3), calculated after alignment to minimized cryo-EM structures using 7-transmembrane bundle Cα atoms. Individual replicate values shown as points. **h-i**, Root-mean-square fluctuation (RMSF) of ICL2 residues P114-R121. Data show mean RMSF ± s.e.m. from three independent 1 µs simulations (n = 3), calculated after alignment using 7-transmembrane bundle Cα atoms. Individual replicate values shown as points. **j**, RMSD distributions of ICL2 (P114-R121) relative to FFA2/TUG-1375/AZ-1729/Gi1 complex. Violin plots show probability densities from 3 simulation replicates per complex. Horizontal bars indicate minimum, maximum, and median values. Percentages indicate proportion of frames with RMSD < 1.5 Å. **k**, Similar analysis using FFA2/TUG-1375/compound 187/miniG_q complex as a reference. **l-n**, Analysis of polar contacts at the TM6-TM7 interface. Violin plots show distributions of inter-atomic distances from snapshots taken every 100 ps across three independent 1 µs simulations per complex. When multiple atoms are selected (e.g., $O^{δ1}$ and $N^{δ2}$ of N230), the shortest distance between residue atoms is shown. Horizontal bars indicate minimum, maximum, and median values. **l**, Distances between $N230^{6.43}$ and $N265^{7.45}$ (D/$NP^{7.50}$xxY motif) with percentage of frames ≤3.5 Å indicated. **m**, Oxygen-to-sulfur distances between $N230^{6.43}$ and $C234^{6.47}$ ($C^{6.47}W^{6.48}xP^{6.50}$ motif) with percentage of frames ≤4.5 Å indicated. **n**, Hydrogen bonds between cytosolic region of TM6 (Q215-N230) and TM7 (R255-Y274). Data show percentage of frames with at least one hydrogen bond present ± s.e.m. from three independent 1 µs simulations (n = 3). Individual replicate values shown as black dots. Conformational stability analysis of FFA2 receptor states can be found in Supplementary Fig. 3. Detailed RMSD and RMSF data for all simulated systems and residue-ligand interaction energy values can be found in Supplementary Tables 1 and 2. Cmpd187 refers to compound 187.

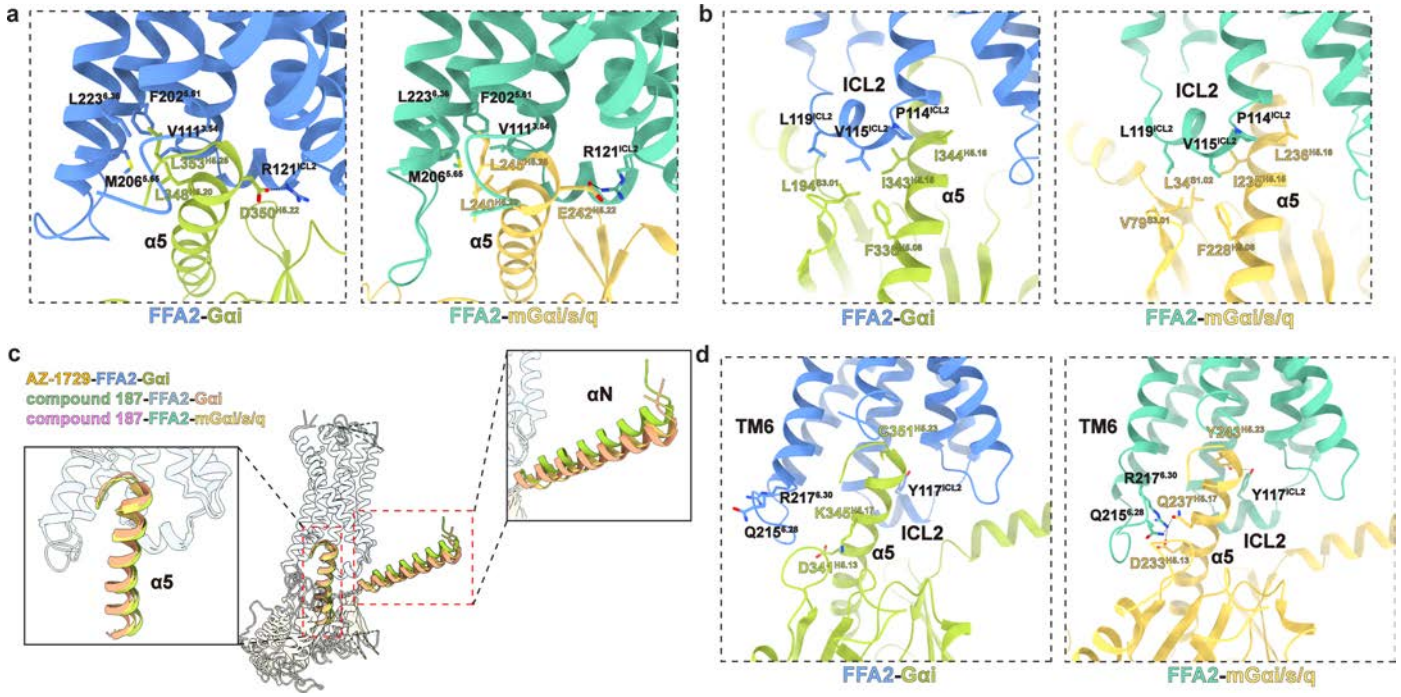

Extended Data Fig. 6 | G protein-coupling to FFA2. a, Interactions between FFA2 and the α5 helix of G_i (from the structure of FFA2 with AZ-1729 and G_i) or miniG_q (from the structure of FFA2 with compound187 and miniG_q). **b**, Interactions between FFA2 and the αN helix of G_i or miniG_q. Polar interactions are shown as black dashed lines. Specifically, in both structures, D350$^{H5.22}$ (G protein numbering) in G_i, or E242$^{H5.22}$ in $mG_{\alpha i/s/q}$ forms a polar interaction with R121^{ICL2} in FFA2. Additionally, L348$^{H5.20}$ and L353$^{H5.25}$ in G_i form hydrophobic interactions with V111$^{3.54}$, F202$^{5.61}$, M206$^{5.65}$, and L223$^{6.36}$ of FFA2, while the corresponding residues, L240$^{H5.20}$ and L245$^{H5.25}$ in $mG_{\alpha i/s/q}$, also form direct interactions with these residues in FFA2. Notably, residues P114^{ICL2}, V115^{ICL2}, and L119^{ICL2} in ICL2 of FFA2 inserts into a hydrophobic pocket formed by G_i residues L194$^{S3.01}$, F336$^{H5.08}$, I343$^{H5.15}$, and I344$^{H5.16}$, or $mG_{\alpha i/s/q}$ residues F228$^{H5.08}$, I235$^{H5.15}$, and L236$^{H5.16}$, stabilizing a significant hydrophobic environment. **c**, Structural comparison of the α5 and αN helices in the TUG-1375-AZ-1729-FFA2-G_i (yellow), TUG-1375-compound187-FFA2-miniG_q (yellow green), and TUG-1375-compound-FFA2-G_i (pink) complexes. The α5 helix adopts a highly similar conformation across all three structures, whereas the αN helix exhibits greater variability. **d**, Polar interactions between FFA2 and the α5 helix of miniG_q (right panel), which are missing in the structures with G_i (left panel). Polar interactions are shown as black dashed lines.

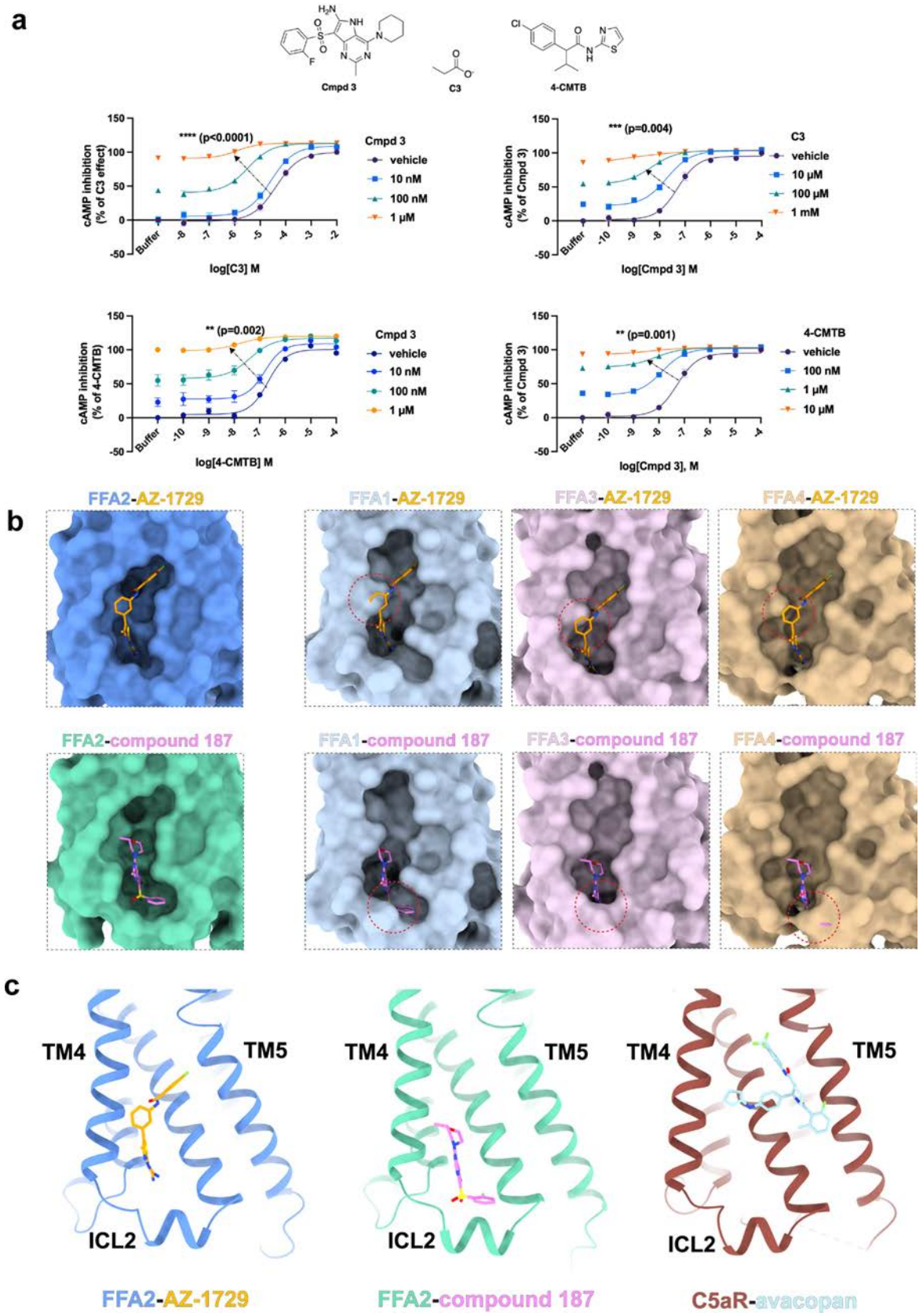

Extended Data Fig. 7 | See next page for caption.

Extended Data Fig. 7 | Compound3 and ligand selectivity at Site 2. a, Effect of various concentrations of compound3 on the concentration-response profiles of 4-CMTB and C3. Assays were performed as described in Methods, with the following adjustments: (1) 2,000 cells were seeded per well; (2) cAMP accumulation was induced by 0.1 μM forskolin; (3) cells were incubated for 45 min with indicated agonists. Error bars represent mean ± s.e.m. from 3 biologically independent experiments, each performed in triplicate. p-values refer to changes in potency and are reported according to one-way ANOVA test with Dunnet's post hoc analysis. **b**, Comparison of Site 2 in FFA2 and similar pockets in FFA1, FFA3, and FFA4. AZ-1729 and compound187 were docked to the other FFAs by aligning their structures to FFA2 structures with these two PAMs. Severe steric clashes as indicated by red circles are observed between AZ-1729 or cmpd187 and other FFAs, indicating a high selectivity of these two PAMs for FFA2. **c**, Comparison of Site 2 in FFA2 and the similar allosteric site in C5aR. *Left*: FFA2 (blue) in complex with the PAM AZ-1729 (orange); *Middle*: FFA2 (green) in complex with the PAM compound187 (pink); *Right*: C5a receptor (C5aR, brown) in complex with the NAM avacopan (light blue). The crystal structure of the C5aR-avacopan complex (PDB ID: 6C1R) illustrates the binding mode of this allosteric antagonist.

Extended Data Table 1 | Cryo-EM data collection, refinement and validation statistics

	TUG-1375-4-CMTB-FFA2-Gq (EMDB-45732) (PDB 9CLW)	TUG-1375-cmpd187-FFA2-Gq (EMDB-45738) (PDB 9CM3)	TUG-1375-AZ-1729-FFA2-Gi (EMDB-45743) (PDB 9CM7)	TUG-1375-cmpd187-FFA2-Gi (EMDB-49745) (PDB 9NS9)
Data collection and processing				
Magnification	105,000	165,000	105,000	165,000
Voltage (kV)	300	300	300	300
Electron exposure (e–/Å^2)	55	55	55	55
Defocus range (μm)	-1.0 to -1.8	-1.0 to -2.0	-1.0 to -1.8	-1.0 to -2.0
Pixel size (Å)	0.828	0.72	0.828	0.72
Symmetry imposed	C1	C1	C1	C1
Initial particle images (no.)	5,172,796	8,058,394	8,630,776	11,047,993
Final particle images (no.)	309,387	348,210	161,839	271,668
Map resolution (Å)	3.26 (receptor) 3.13 (G protein)	3.06 (overall)	3.37 (receptor) 3.23 (G protein)	3.38 (receptor) 3.21 (G protein)
FSC threshold	0.143	0.143	0.143	0.143
Map resolution range (Å)	2.2-4.5	2.2-4.5	2.2-4.5	2.2-4.5
Refinement				
Initial model used (PDB code)	8T3S	8T3S	8G05	8G05
Model resolution (Å)	3.4	3.2	3.4	3.5
FSC threshold	0.5	0.5	0.5	0.5
Map sharpening *B* factor (Å^2)	-145.7	-130.3	-138.4	-150.6
Model composition				
Non-hydrogen atoms	9001	8845	8791	8357
Protein residues	1130	1130	1124	1116
Ligands	2	2	2	2
B factors (Å^2)				
Protein	110.19	77.79	102.56	98.43
Ligand	57.06	40.76	66.88	59.62
R.m.s. deviations				
Bond lengths (Å)	0.005	0.002	0.003	0.002
Bond angles (°)	0.829	0.465	0.527	0.575
Validation				
MolProbity score	1.78	1.48	1.64	1.60
Clashscore	9.94	6.58	8.68	8.52
Poor rotamers (%)	0.42	0.21	0.11	0.48
Ramachandran plot				
Favored (%)	96.14	97.39	97.02	97.27
Allowed (%)	3.86	2.61	2.98	2.73
Disallowed (%)	0	0	0	0

Cryo-EM data collection, model refinement and validation statistics for the four TUG-1375-bound FFA2 signaling complexes. Cmpd187 refers to compound 187.

Extended Data Table 2 | Effects of mutations in Site 1 and Site 2 on the action of FFA2 ligands

a

	TUG-1375		AZ-1729		4-CMTB		cmpd187	
	pEC_{50} ± SEM	Emax ± SEM	pEC_{50} ± SEM	Emax ± SEM	pEC_{50} ± SEM	Emax ± SEM	pEC_{50} ± SEM	Emax ± SEM
FFA2-WT	7.47 ± 0.12	100	7.55 ± 0.11	146 ± 14***	6.11 ± 0.02	98 ± 5	8.47 ± 0.11	89 ± 5
N230D	7.50 ± 0.13	100	7.50 ± 0.14	116 ± 4	NR	NR	8.39 ± 0.04	73 ± 7**
N230S	7.85 ± 0.04	100	8.66 ± 0.21***	113 ± 11	NR	NR	9.09 ± 0.12**	72 ± 15
V226A	7.56 ± 0.10	100	7.75 ± 0.15	188 ± 14****	5.75 ± 0.26	48 ± 8**	8.76 ± 0.15	94 ± 12
F261L	7.72 ± 0.11	100	7.87 ± 0.03	137 ± 5****	6.43 ± 0.24	103 ± 8	8.49 ± 0.08	87 ± 2

b

	TUG-1375 pEC50 ± SEM	AZ-1729 pEC50 ± SEM	4-CMTB pEC50 ± SEM	cmpd187 pEC50 ± SEM
FFA2-WT	6.72 ± 0.06	6.03 ± 0.01	5.18 ± 0.10	7.60 ± 0.05
L47Y	6.09 ± 0.05**	5.50 ± 0.12	5.31 ± 0.08	NR
G102V	6.72 ± 0.16	>4	5.20 ± 0.04	6.55 ± 0.16*
E106G	6.54 ± 0.14	NR	5.37 ± 0.16	NR
Y117F	6.53 ± 0.10	5.78 ± 0.02	5.23 ± 0.17	7.20 ± 0.14
G126S	6.46 ± 0.06	>4	5.48 ± 0.04	5.54 ± 0.41***
A129V	6.63 ± 0.04	5.50 ± 0.08	5.22 ± 0.19	6.40 ± 0.11*

c

	TUG-1375		AZ-1729		4-CMTB		cmpd187	
	pEC_{50} ± SEM	Emax ± SEM	pEC_{50} ± SEM	Emax ± SEM	pEC_{50} ± SEM	Emax ± SEM	pEC_{50} ± SEM	Emax ± SEM
FFA2-WT	7.76 ± 0.06	100	7.97 ± 0.09	116 ± 1	6.49 ± 0.08	101 ± 7	8.59 ± 0.17	88 ± 8
L47Y	6.89 ± 0.09****	100	6.64 ± 0.11****	137 ± 4**	6.29 ± 0.09	92 ± 8	NR	NR
G102V	7.73 ± 0.10	100	6.26 ± 0.03****	103 ± 5	6.53 ± 0.13	98 ± 3	7.24 ± 0.11****	79 ± 4**
E106G	7.69 ± 0.09	100	8.10 ± 0.08	56 ± 4 ****	6.48 ± 0.08	83 ± 6*	8.58 ± 0.17	33 ± 1****
L109A	7.59 ± 0.12	100	7.00 ± 0.09**	135 ± 13	6.24 ± 0.02	75 ± 5	7.00 ± 0.10****	50 ± 2*
L109V	7.94 ± 0.07	100	7.82 ± 0.11	112 ± 5	6.28 ± 0.05	98 ± 3	6.89 ± 0.02****	69 ± 2***
F113A	7.53 ± 0.15	100	7.06 ± 0.18**	149 ± 6*	6.17 ± 0.03	89 ± 14	7.70 ± 0.17****	92 ± 9
Q116A	7.66 ± 0.07	100	7.80 ± 0.05	145 ± 11*	6.00 ± 0.07*	113 ± 10	8.36 ± 0.08	93 ± 9
Y117A	6.89 ± 0.01****	100	5.90 ± 0.08****	150 ± 13*	5.47 ± 0.07****	104 ± 12	6.78 ± 0.13****	129 ± 5
Y117F	7.93 ± 0.09	100	7.72 ± 0.08	99 ± 3	6.59 ± 0.03	93 ± 6	8.49 ± 0.13	78 ± 3**
S120E	7.89 ± 0.09	100	7.24 ± 0.10*	117 ± 12	6.50 ± 0.11	96 ± 8	8.76 ± 0.11	87 ± 9
S120F	7.99 ± 0.17	100	7.80 ± 0.21	105 ± 5	6.44 ± 0.13	106 ± 2	8.66 ± 0.05	89 ± 2
R121A	7.16 ± 0.03****	100	6.46 ± 0.14****	200 ± 20***	5.67 ± 0.05****	105 ± 10	7.97 ± 0.03***	126 ± 10
Y125Q	7.80 ± 0.08	100	7.55 ± 0.06	126 ± 4*	6.56 ± 0.07	92 ± 8	8.88 ± 0.11	96 ± 8
G126S	7.32 ± 0.08**	100	6.13 ± 0.32****	84 ± 8 ***	6.28 ± 0.05	89 ± 2	NR	NR
A129V	7.70 ± 0.05	100	6.48 ± 0.53****	113 ± 2*	6.58 ± 0.02	97 ± 4	7.31 ± 0.10****	70 ± 2***

a, Effects of mutations in Site 1 on the potency and efficacy of FFA2 modulators measured in [^{35}S]GTPγS assays. Emax calculated as % of TUG-1375 response. **b**, Effects of mutations in Site 2 on potency of FFA2 modulators measured by cAMP assays. **c**, Effects of mutations in Site 2 on the potency and efficacy of FFA2 modulators measured by [^{35}S]GTPγS binding assays. Emax calculated as % of TUG-1375 response. In all tables, statistical significance was assessed by one way ANOVA followed by Dunnett's multiple comparison test. Data are means +/– s.e.m. n=3 (three biologically independent experiments). * $p<0.05$, ** $p<0.01$, *** $p<0.001$, **** $p<0.0001$. NR, no detectable response. Cmpd187 refers to compound 187.

nature portfolio

Corresponding author(s): Irina G. Tikhonova, Graeme Milligan, Cheng Zhang

Last updated by author(s): May 12, 2025

Reporting Summary

Nature Portfolio wishes to improve the reproducibility of the work that we publish. This form provides structure for consistency and transparency in reporting. For further information on Nature Portfolio policies, see our Editorial Policies and the Editorial Policy Checklist.

Statistics

For all statistical analyses, confirm that the following items are present in the figure legend, table legend, main text, or Methods section.

n/a	Confirmed
☐	☒ The exact sample size (*n*) for each experimental group/condition, given as a discrete number and unit of measurement
☐	☒ A statement on whether measurements were taken from distinct samples or whether the same sample was measured repeatedly
☐	☒ The statistical test(s) used AND whether they are one- or two-sided *Only common tests should be described solely by name; describe more complex techniques in the Methods section.*
☒	☐ A description of all covariates tested
☒	☐ A description of any assumptions or corrections, such as tests of normality and adjustment for multiple comparisons
☐	☒ A full description of the statistical parameters including central tendency (e.g. means) or other basic estimates (e.g. regression coefficient) AND variation (e.g. standard deviation) or associated estimates of uncertainty (e.g. confidence intervals)
☐	☒ For null hypothesis testing, the test statistic (e.g. *F*, *t*, *r*) with confidence intervals, effect sizes, degrees of freedom and *P* value noted *Give P values as exact values whenever suitable.*
☒	☐ For Bayesian analysis, information on the choice of priors and Markov chain Monte Carlo settings
☒	☐ For hierarchical and complex designs, identification of the appropriate level for tests and full reporting of outcomes
☒	☐ Estimates of effect sizes (e.g. Cohen's *d*, Pearson's *r*), indicating how they were calculated

Our web collection on statistics for biologists contains articles on many of the points above.

Software and code

Policy information about availability of computer code

Data collection	SerialEM 4.0, EPU3.7 , AMBER20, Schrodinger Maestro 2021-3, NAMDGit-2017-12-19, Linux-x86_64-multicore-CUDA
Data analysis	cryoSPARC 4.2, COOT 0.9.8.7, Phenix 1.21.2, ChimeraX-1.9, Prism 10, Schrodinger GLIDE, Schrodinger Maestro 2021-3 suite, CHARMM-GUI, AmberTools23, MDAnalysis 2.7.0, SciKit Learn, 1.5.1 VMD1.9.3 , Pymol 3.0.5, NumPy, 1.26.4 SciPy1.14.0, MatPlotLib 3.9.1, Seaborn 0.13.2, Python 3.12.4, ParmEd 3.4.4, NAMD2, HTMD2.3.2/2.3.36, PackMol 20.01

For manuscripts utilizing custom algorithms or software that are central to the research but not yet described in published literature, software must be made available to editors and reviewers. We strongly encourage code deposition in a community repository (e.g. GitHub). See the Nature Portfolio guidelines for submitting code & software for further information.

Data

Policy information about availability of data

All manuscripts must include a data availability statement. This statement should provide the following information, where applicable:

- Accession codes, unique identifiers, or web links for publicly available datasets
- A description of any restrictions on data availability
- For clinical datasets or third party data, please ensure that the statement adheres to our policy

The 3D cryo-EM density maps of the structures of FFA2 signaling complexes have been deposited in the Electron Microscopy Data Bank under the accession numbers EMD-45732 (https://www.ebi.ac.uk/emdb/EMD-45732) for TUG-1375-4-CMTB-FFA2-miniGq, EMD-45738 (https://www.ebi.ac.uk/emdb/EMD-45738) for

TUG-1375-cmpd187-FFA2-miniGq, EMD-45743 (https://www.ebi.ac.uk/emdb/EMD-45743) for TUG-1375-AZ-1729-FFA2-Gi, and EMD-49745 (https://www.ebi.ac.uk/emdb/EMD-49745) for TUG-1375-cmpd187-FFA2-Gi. Atomic coordinates for the atomic models have been deposited in the Protein Data Bank (PDB) under the accession numbers 9CLW (https://doi.org/10.2210/pdb9CLW/pdb) for TUG-1375-4-CMTB-FFA2-miniGq, 9CM3 (https://doi.org/10.2210/pdb9CM3/pdb) for TUG-1375-cmpd187-FFA2-miniGq, 9CM7 (https://doi.org/10.2210/pdb9CM7/pdb) for TUG-1375-AZ-1729-FFA2-Gi, and 9NS9 (https://doi.org/10.2210/pdb9NS9/pdb) for TUG-1375-cmpd187-FFA2-Gi.
The following structural data used for comparison are available in the Protein Data Bank (PDB): 7LD3 (https://doi.org/10.2210/pdb7LD3/pdb, the adenosine A1 receptor bound to the PAM MIPS521) 38, 8J22 (https://doi.org/10.2210/pdb8J22/pdb, TUG-1375-bound FFA2 coupled with Gi) 22, 8J23 (https://doi.org/10.2210/pdb8J23/pdb, empty FFA2 coupled with Gi), 8T3S (https://doi.org/10.2210/pdb8T3S/pdb, butyrate-bound FFA2 coupled with miniGq) 21, 8J21 (https://doi.org/10.2210/pdb8J21/pdb, butyrate-bound FFA3 coupled with Gi) 22, 8G05 (https://doi.org/10.2210/pdb8G05/pdb, GPR84 coupled with Gi) 85, 6C1R (https://doi.org/10.2210/pdb6C1R/pdb, C5aR bound to PMX53 and avacopan) 59.
Simulation trajectories were uploaded to GPCRmd (https://www.gpcrmd.org/) 86 and linked to the current publication. Simulation IDs are provided in Supplementary Table 3.

Research involving human participants, their data, or biological material

Policy information about studies with human participants or human data. See also policy information about sex, gender (identity/presentation), and sexual orientation and race, ethnicity and racism.

Reporting on sex and gender	N/A
Reporting on race, ethnicity, or other socially relevant groupings	N/A
Population characteristics	N/A
Recruitment	N/A
Ethics oversight	N/A

Note that full information on the approval of the study protocol must also be provided in the manuscript.

Field-specific reporting

Please select the one below that is the best fit for your research. If you are not sure, read the appropriate sections before making your selection.

☒ Life sciences ☐ Behavioural & social sciences ☐ Ecological, evolutionary & environmental sciences

For a reference copy of the document with all sections, see nature.com/documents/nr-reporting-summary-flat.pdf

Life sciences study design

All studies must disclose on these points even when the disclosure is negative.

Sample size	For functional assays, we used data from 3-5 experiments. The rational is that three biological replicates are the minimum for inferential analysis. For cryo-EM studies, each dataset contains 10 to 20 million particles, collected from >10,000 micrographs. The sample size was determined based on the number of particles to achieve sufficient resolition of cryo-EM maps.
Data exclusions	For cryo-EM data, particles were excluded during 2D and 3D classification based on protocols of cryoSparc to achieve high resolution.
Replication	For all signaling and binding assays, we used data from 3-5 repeated experiments . Not all attempts at replication were successful because of mistakes in sample preparation. For each cryo-EM structure, 4-6 cryo-grids prepared from the same protein sample were screened and the best grid was used fro data collection. Only one cryo-EM dataset was used for the determination of each structure. Classical MD simulations included 3 replicates, probe-confined dynamic mapping included 5 replicates.
Randomization	All experiments follow a deterministic pattern. No probability distributions were involved in the rationale of experimental design. All the pharmacological data for replication and statistical analysis were obtained using distinct biological replicates from membrane preparations from different cell cultures.
Blinding	No human or animal subjects are involved. Blinding is not applicable to the study. All experiments follow a deterministic pattern. The investigators were aware of how cells were treated before collecting data and how protein samples were prepared for cryo-EM data collection.

Reporting for specific materials, systems and methods

We require information from authors about some types of materials, experimental systems and methods used in many studies. Here, indicate whether each material, system or method listed is relevant to your study. If you are not sure if a list item applies to your research, read the appropriate section before selecting a response.

Materials & experimental systems

n/a	Involved in the study
☒	☐ Antibodies
☐	☒ Eukaryotic cell lines
☒	☐ Palaeontology and archaeology
☒	☐ Animals and other organisms
☒	☐ Clinical data
☒	☐ Dual use research of concern
☒	☐ Plants

Methods

n/a	Involved in the study
☒	☐ ChIP-seq
☒	☐ Flow cytometry
☒	☐ MRI-based neuroimaging

Eukaryotic cell lines

Policy information about cell lines and Sex and Gender in Research

Cell line source(s)	Flp-In™ T-REx™ 293 cells (InvitroGen), HEK293T cells (ATCC), insect Sf9 cells (ExpressionSystems)
Authentication	All the mammalian cell lines are fully authenticated. We rely on the vendor to authenticate the insect cell line.
Mycoplasma contamination	HEK293T and Flp-In T-REx 293 cells were authenticated by Northgene (Case Number C-24809a and C-24809b). They were confirmed to be mycoplasma free and continue to be tested for mycoplasma every 3 months.
Commonly misidentified lines (See ICLAC register)	None found in the ICLAC database.

Plants

Seed stocks	N/A
Novel plant genotypes	N/A
Authentication	N/A